International Journal of Fracture **93:** 115–144, 1998.

A single-domain dual-boundary-element formulation incorporating a cohesive zone model for elastostatic cracks

B. YANG and K. RAVI-CHANDAR
Department of Mechanical Engineering, University of Houston, Houston, Tx 77204-4792, U.S.A.
e-mail: ravi@uh.edu

Received 11 December 1997; accepted in revised form 19 June 1998

Abstract. A cracked elastostatic structure is artificially divided into subdomains of simpler topology such that the well-developed classic dual integral equations can be applied appropriately to each domain. Applying the continuity and equilibrium conditions along artificial boundaries and properties of the integral kernels a single-domain dual-boundary-integral equation formulation is derived for a cracked elastic structure. A cohesive zone model is used to model the crack tip processes and is coupled with the single-domain dual-boundary-integral equation formulation; the resulting nonlinear equations are solved using the iterative method of successive-over-relaxation. The constitutive law used for a crack includes three parts: a law relating cohesive force to crack displacement difference when a crack is opening, a characterization of tangential interaction between crack surfaces when the crack surfaces are in contact, and a maximum principal stress criterion of crack advance. Incorporation of local unloading effect of the cohesive zone material has enabled a simulation of fracture with initial damage, partial development of the failure process zone at structural instability and multiple crack interaction. Some of the features of the method are demonstrated by considering three examples. The first problem is a single-edge-cracked specimen that exhibits a snap-back instability. The second example is the development of wing cracks from an angled crack under compression. The last example demonstrates the capability to consider mixed-mode crack growth and interaction of cracks. Thus, the problem of crack growth has been reduced to the determination of the cohesive model for the fracture process.

Key words: Cohesive zone model, boundary integral method.

1. Introduction

Boundary element method (BEM) has received much attention recently, especially in application to fracture mechanics (FM) (see Cruse, 1996 and Aliabadi, 1997 for reviews). The method is attractive because it involves discretization of the boundary alone; the dimensionality of the stiffness matrix formed in BEM is then reduced by one in comparison to a domain method, such as finite element method (FEM), although the stiffness matrix is full and asymmetric in general. A particularly attractive advantage of BEM in application to crack problems over FEM is that domain remeshing is not necessary when a crack grows; only one more element of a crack is added with all the already existing elements untouched. However, as a crack is modeled mathematically with the two crack surfaces being coincident, the classic boundary integral equation (BIE) can not be applied directly or the resulting stiffness matrix formed will be ill-conditioned. A great deal of effort has been expended in dealing with this difficulty; many methods – such as the crack Green's function method (Snyder and Cruse, 1975), the displacement discontinuity method (Crouch, 1976 and Wen, 1996), the subdomains method (Blandford, Ingraffea and Liggett, 1981), the dual boundary element method (DBEM) (Hong and Chen, 1988, Portela, Aliabadi and Rooke, 1992, and Chen and Chen,

1995), the single-domain traction boundary element method (Young, 1996), and some hybrid methods optimizing the advantages of some of the above mentioned methods (Ameen and Raghuprasad, 1994) – have been proposed. It is not our intent to review these methods here; one may see Chen and Chen (1995) for a discussion of some of these methods. Among the methods mentioned above the method of subdomains eliminates the discrepancy noted above by cutting a cracked structure into pieces of simpler topology such that BIE can be applied properly to each of domain separately. However, this formulation increases the computational effort as a result of the additional artificial boundaries that appear from the cutting process; moreover, when a crack advances, remeshing is still needed in general. Nevertheless, the idea of the method of subdomains is valuable and is adopted in the present paper to derive a mathematically rigorous and simple formulation of the *single-domain dual-boundary-integral equations* (SDDBIEs) of a cracked structure. The classic dual integral equations for a simple structure is, of course, well established in the literature. These SDDBIEs were given by Young (1996), and applied to solve a traction-free crack problem using continuous elements.

The present paper is organized as follows: In Section 2, we summarize the classic dual integral equations for a simple elastostatic structure, and derive the single-domain dual-integral-equations for an elastostatic structure containing a mathematically modeled crack. By applying continuity conditions and properties of the integral kernels across the cut, the integrals along the artificial boundaries that appear due to cutting are eliminated. In most crack problems in which tractions on two opposite crack surfaces are equal in magnitude and opposite in directions, the single-domain dual-boundary-integral equations can be further simplified with integrals of crack tractions eliminated. In Section 3, we consider the problem of a cohesive crack. A line spring model is used to characterize interaction between two cohesive crack surfaces opening or sliding. Material softening with accumulated damage is also incorporated into the cohesive model. This model seems most appropriate to a crazing zone in polymers, in which the bridging long chain molecules are fully orientated and flexible, but can also be applied to most bridged crack problems, such as in ceramics and fiber or particle reinforced materials.

Coulomb friction law is applied to crack surfaces when they come in contact due to normal pressure. This line spring model may contribute to tangential interaction too if not broken completely in that case. The maximum principal stress criterion is applied for the marching of an existing crack. A physical crack tip would follow along the same path as a natural result of complete debonding of the cohesive zone material behind the fictitious crack tip. Note that the incorporation of local unloading effect of the cohesive zone material has enabled a simulation of fracture with an initial process zone, the partial development at structural instability and most importantly arbitrary crack interaction. In Section 4, we introduce an iterative boundary element method of successive over-relaxation to approach numerically the problem of a cohesive crack formulated in Section 3. An iterative process is necessary in the present problem since behavior of the cohesive zone material is nonlinear and history dependent. Crack opening and contact are both programmed simply in the iterative process. No special iterative procedure is needed for mixed crack opening and contact problem. In Section 5, we simulate a two-dimensional rectangular specimen with three different crack configurations. Problems involving structural instability, mixed-mode crack growth, crack surface compression and friction and multiple crack interactions are all explored as examples demonstrating the power of the cohesive zone formulation of the boundary element method.

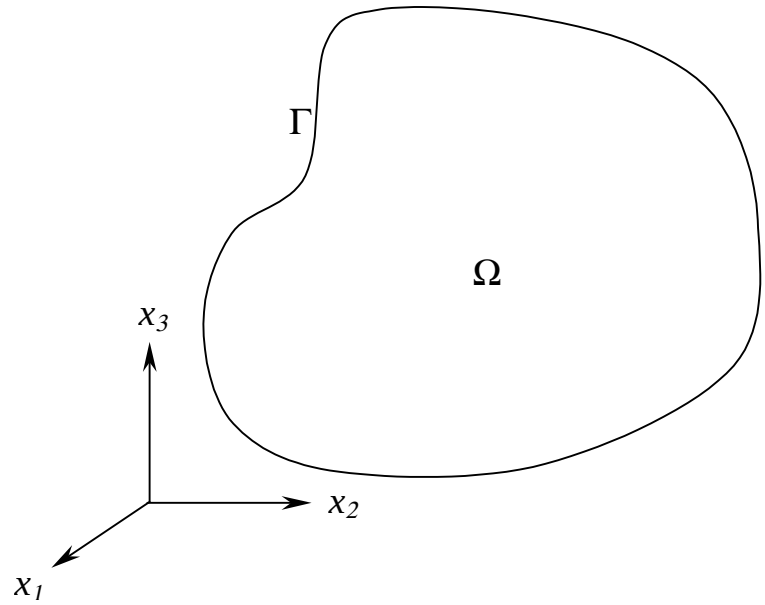

Figure 1. An isotropic, homogeneous, linear elastic domain Ω with boundary Γ.

2. Single-domain dual boundary integral equations of a cracked structure in elastostatics

2.1. Summary of the dual integral equations for a simple structure

Consider a homogeneous, isotropic, linearly elastic domain Ω with piecewise smooth boundary Γ as shown in Figure 1. A Cartesian (Lagrangian) coordinate system[1] is used along with standard indicial notation. The displacement components $u_i(\mathbf{X})$, at a point $\mathbf{X}$, can be represented in the following form

$$\underline{c}_{ij}(\mathbf{X})u_j(\mathbf{X}) = \int_\Gamma \{u^*_{ij}(\mathbf{X},\mathbf{x})p_j(\mathbf{x}) - p^*_{ij}(\mathbf{X},\mathbf{x},\mathbf{n})u_j(\mathbf{x})\}\,\mathrm{d}\Gamma(\mathbf{x}) + \int_\Omega u^*_{ij}(\mathbf{X},\mathbf{x})b_j(\mathbf{x})\,\mathrm{d}\Omega(\mathbf{x}), \tag{1}$$

where p_j are traction components, b_j are body force components. u^*_{ij} and p^*_{ij} are the fundamental solutions representing the displacements and tractions respectively in the jth direction at a field point $\mathbf{x}$ due to a unit force acting in the ith direction at a source point $\mathbf{X}$. Note that p^*_{ij} are taken along the outward normal vector, $\mathbf{n}$, of Γ at $\mathbf{x}$ and that with the inclusion of $\mathbf{n}$ in

[1] Standard index notation is used. The range for Latin subscript indices is 3 and the range for Greek subscript indices is 2. Summation over repeated subscripts over their range is implied unless suspended explicitly. Superscripts do not follow this range and summation convention; their range would be indicated explicitly and summation is indicated by the summation symbol.

p^*_{ij}, the dependence of the integrals on the normal is made explicit. c_{ij} is a coefficient matrix given by

$$\underline{c}_{ij} = \begin{cases} \delta_{ij} & \mathbf{X} \in \Omega, \\ c_{ij} & \mathbf{X} \in \Gamma, \\ 0 & \text{otherwise}, \end{cases} \tag{2}$$

where δ_{ij} is Kronecker delta, and $c_{ij} = \delta_{ij}/2$ if the tangential surface at $\mathbf{X}$ is smooth; if it is not the case one may see Hartmann (1980) for the closed-form expressions of this matrix. When $\mathbf{X} \in \Omega$, (1) with $\underline{c}_{ij} = \delta_{ij}$ is called the *Somigliana identity*. One may easily prove that, if $\mathbf{X}$ is outside Ω and Γ, (1) holds trivially with $\underline{c}_{ij} = 0$. The form of (1) most useful in the boundary integral formulation arises when $\mathbf{X} \in \Gamma$. Applying a limiting process as $\mathbf{X}$ approaches a boundary, the Somigliana identity leads to the boundary integral equation of displacements (BIED, or usually BIE), based on which the classic boundary element technique is developed (Brebbia, Telles and Wrobel, 1984).

Differentiating (1) with respect to $\mathbf{X}$ (with $\mathbf{X} \in \Omega$) the strains over Ω can be calculated. If these strains are substituted into Hooke's law, the integral equations of stresses at a source point $\mathbf{X}$ (with $\mathbf{X} \in \Omega$) are obtained. A limiting process, similar to the one used to obtain the BIE, can be applied to the resulting integral equation as $\mathbf{X}$ approaches a boundary, leading to the boundary integral equation of stresses. These integral equations are summarized below

$$\begin{aligned} \underline{C}_{ik}(\mathbf{X})\sigma_{kj}(\mathbf{X}) \;=\; & \int_\Gamma \{U^*_{ijk}(\mathbf{X}, \mathbf{x})\, p_k(\mathbf{x}) - P^*_{ijk}(\mathbf{X}, \mathbf{x}, \mathbf{n}) u_k(\mathbf{x})\}\, \mathrm{d}\Gamma(\mathbf{x}) \\ & + \int_\Omega U^*_{ijk}(\mathbf{X}, \mathbf{x}) b_k(\mathbf{x})\, \mathrm{d}\Omega(\mathbf{x}), \end{aligned} \tag{3}$$

where U^*_{ijk} and P^*_{ijk} are linear combinations of derivatives of u^*_{ij} and p^*_{ij}, with respect to $\mathbf{X}$. As in the case of p^*_{ij}, P^*_{ijk} are taken along the outward normal vector, $\mathbf{n}$, of Γ at $\mathbf{x}$. $\underline{C}_{ij}$ is a coefficient matrix given by

$$\underline{C}_{ij} = \begin{cases} \delta_{ij} & \mathbf{X} \in \Omega, \\ \delta_{ij}/2 & \mathbf{X} \in \Gamma, \\ 0 & \text{otherwise}, \end{cases} \tag{4}$$

which is identical to $\underline{c}_{ij}$ provided that corner points where tractions are not well defined are excluded. If (3) are multiplied on both sides by the outward normal vector at $\mathbf{X}$ as $\mathbf{X}$ in Γ, then, the boundary integral equations of tractions (BIET) are obtained, which may be employed to formulate a boundary element method in a similar way as BIE.

The fundamental solutions used in the above formulation are due to Kelvin (Love, 1944), and are the basic singular solutions to a point load in an infinite medium. The components u^*_{ij} and p^*_{ij} are given below for two (plane-strain) and three-dimensional problems:

$$u^*_{ij}(\mathbf{X}, \mathbf{x}) = \frac{1}{16\pi\mu(1-\nu)r}[(3-4\nu)\delta_{ij} + r_{,i}r_{,j}], \qquad \text{(3-D)}, \tag{5}$$

$$u^*_{ij}(\mathbf{X}, \mathbf{x}) = \frac{1}{8\pi\mu(1-\nu)}\left[(3-4\nu)\ln\left(\frac{1}{r}\right)\delta_{ij} + r_{,i}r_{,j}\right], \qquad \text{(2-D; plane-strain)}, \tag{6}$$

$$p^*_{ij}(\mathbf{X}, \mathbf{x}, \mathbf{n})$$

$$= \frac{-1}{4\overline{\alpha}\pi(1-\nu)r^{\overline{\alpha}}}\left[\frac{\partial r}{\partial n}((1-2\nu)\delta_{ij} + \overline{\beta}r_{,i}r_{,j}) - (1-2\nu)(r_{,i}n_j - r_{,j}n_i)\right], \tag{7}$$

where μ is shear modulus, and ν is Poisson ratio; $\overline{\alpha} = 2$, $\overline{\beta} = 3$ for three-dimensional problems and $\overline{\alpha} = 1$, $\overline{\beta} = 2$ for two-dimensional plane-strain problems. Moreover, $r = r(\mathbf{X}, \mathbf{x})$ represents the distance between the points $\mathbf{X}$ and $\mathbf{x}$, and its derivatives are taken with respect to $\mathbf{x}$. U^*_{ijk} and P^*_{ijk} are given by

$$U^*_{ijk}(\mathbf{X}, \mathbf{x}) = \frac{1}{4\overline{\alpha}\pi(1-\nu)r^{\overline{\alpha}}}[(1-2\nu)(r_{,j}\delta_{ik} + r_{,i}\delta_{jk} - r_{,k}\delta_{ij}) + \overline{\beta}r_{,i}r_{,j}r_{,k}], \tag{8}$$

$$P^*_{ijk}(\mathbf{X}, \mathbf{x}, \mathbf{n})$$

$$= \frac{\mu}{2\overline{\alpha}\pi(1-\nu)r^{\overline{\beta}}}\left\{\overline{\beta}\frac{\partial r}{\partial n}[(1-2\nu)r_{,k}\delta_{ij} + \nu(r_{,i}\delta_{jk} + r_{,j}\delta_{ik}) - \overline{\gamma}r_{,i}r_{,j}r_{,k}]\right.$$

$$+\overline{\beta}\nu(r_{,i}n_jr_{,k} + n_ir_{,j}r_{,k})$$

$$\left.+(1-2\nu)(\overline{\beta}n_kr_{,i}r_{,j} + n_j\delta_{ik} + n_i\delta_{jk}) - (1-4\nu)n_k\delta_{ij}\right\}, \tag{9}$$

where $\overline{\alpha}$ and $\overline{\beta}$ are as given above, and $\overline{\gamma} = 5$ for three-dimensional problems and $\overline{\gamma} = 4$ for two-dimensional problems. The plane strain expressions are valid for plane stress provided that ν is replaced by $\overline{\nu} = \nu/(1+\nu)$. As a source point $\mathbf{X}$ and a field point $\mathbf{x}$ coincide on a boundary, the integral kernels of u^*_{ij}, p^*_{ij}, U^*_{ijk}, and P^*_{ijk} may be singular and even hypersingular. The corresponding integrals in (1) and (3) are taken in the sense of Cauchy principal value if singular, and are taken in the sense of Hadamard principal value if hypersingular.

2.2. The single-domain dual integral equations for a cracked structure

A structure containing a mathematically sharp crack degenerates the boundary integral formulation due to coincidence of the two crack surfaces. In that case, one cannot apply either BIED or BIET to produce a boundary element method directly in general. This problem has been addressed in a number of ways: partitioning the domain into multi-domains, using crack Green's functions, the displacement discontinuity technique, and so on. In this section, we describe the formulation of a single-domain dual-boundary-integral method using Kelvin's solutions. We cut a cracked elastostatic structure into subdomains of simple topology so that the dual integral equations for a simple structure can be applied to each domain appropriately. In a further step, using the continuity and equilibrium conditions along artificial boundaries, as well as some properties of the integral kernels, we eliminate entirely the integrals involving any artificial boundaries. In order to illustrate the derivation of the single-domain integral equations, we shall consider a structure containing one crack; however, the same approach can be applied to any number of cracks in the structure. Furthermore, for simplicity, we shall ignore the body forces; if necessary, they may be added back into the final equations without any difficulty.

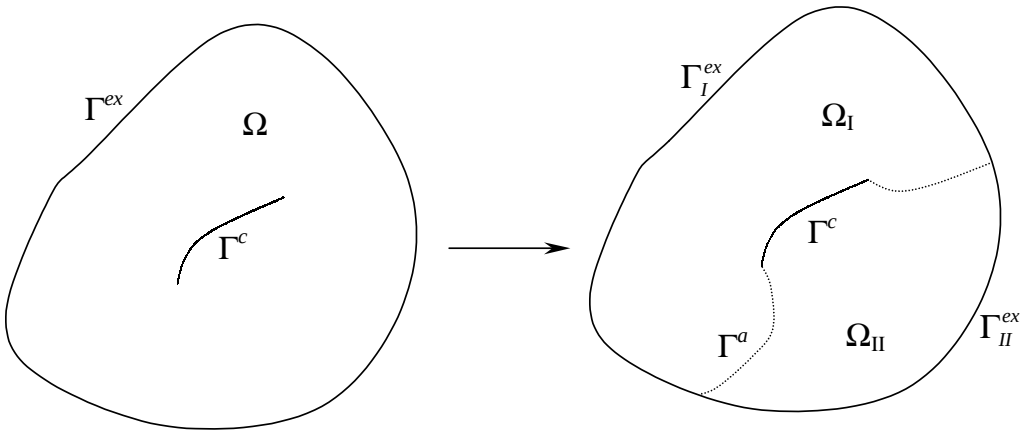

Figure 2. A domain Ω containing a crack Γ^c is cut into two subdomains $\Omega_{\rm I}$ and $\Omega_{\rm II}$ along the dotted line path Γ^a.

As shown in Figure 2, a structure containing one crack is cut into two subdomains with a path that passes through the crack. We denote the two subdomains without a crack by $\Omega_{\rm I}$ and $\Omega_{\rm II}$ respectively. Their boundaries are denoted by $\Gamma_{\rm I}$ and $\Gamma_{\rm II}$ respectively. The topology of the subdomains is simple such that (1) and (3) may be applied to them. This results in the following sets of equations for the displacement and traction components in the two subdomains. For the domain $\Omega_{\rm I}$, we have

$$\underline{c}^{\rm I}_{ij}(\mathbf{X})u^{\rm I}_j(\mathbf{X}) = \int_{\Gamma_{\rm I}} \{u^*_{ij}(\mathbf{X},\mathbf{x})\,p^{\rm I}_j(\mathbf{x}) - p^*_{ij}(\mathbf{X},\mathbf{x},\mathbf{n}^{\rm I})u^{\rm I}_j(\mathbf{x})\}\,{\rm d}\Gamma(\mathbf{x}), \tag{10}$$

with

$$\underline{c}^{\rm I}_{ij} = \begin{cases} \delta_{ij} & \mathbf{X}\in\Omega_{\rm I}, \\ c^{\rm I}_{ij} & \mathbf{X}\in\Gamma_{\rm I}, \\ 0 & \text{otherwise} \end{cases} \tag{11}$$

and

$$\underline{C}^{\rm I}_{ik}(\mathbf{X})\sigma^{\rm I}_{kj}(\mathbf{X}) = \int_{\Gamma_{\rm I}} \{U^*_{ijk}(\mathbf{X},\mathbf{x})\,p^{\rm I}_k(\mathbf{x}) - P^*_{ijk}(\mathbf{X},\mathbf{x},\mathbf{n}^{\rm I})u^{\rm I}_k(\mathbf{x})\}\,{\rm d}\Gamma(\mathbf{x}), \tag{12}$$

with

$$\underline{C}^{\rm I}_{ik} = \begin{cases} \delta_{ik} & \mathbf{X}\in\Omega_{\rm I}, \\ \delta_{ik}/2 & \mathbf{X}\in\Gamma_{\rm I}, \\ 0 & \text{otherwise.} \end{cases} \tag{13}$$

For the domain $\Omega_{\rm II}$, we also have

$$\underline{c}^{\rm II}_{ij}(\mathbf{X})u^{\rm II}_j(\mathbf{X}) = \int_{\Gamma_{\rm II}} \{u^*_{ij}(\mathbf{X},\mathbf{x})\,p^{\rm II}_j(\mathbf{x}) - p^*_{ij}(\mathbf{X},\mathbf{x},\mathbf{n}^{\rm II})u^{\rm II}_j(\mathbf{x})\}\,{\rm d}\Gamma(\mathbf{x}), \tag{14}$$

with

$$\underline{c}_{ij}^{\mathrm{II}} = \begin{cases} \delta_{ij} & \mathbf{X} \in \Omega_{\mathrm{II}}, \\ c_{ij}^{\mathrm{II}} & \mathbf{X} \in \Gamma_{\mathrm{II}}, \\ 0 & \text{otherwise}, \end{cases} \tag{15}$$

and

$$\underline{C}_{ik}^{\mathrm{II}}(\mathbf{X})\sigma_{kj}^{\mathrm{II}}(\mathbf{X}) = \int_{\Gamma_{\mathrm{II}}} \{U_{ijk}^{*}(\mathbf{X}, \mathbf{x}) p_k^{\mathrm{II}}(\mathbf{x}) - P_{ijk}^{*}(\mathbf{X}, \mathbf{x}, \mathbf{n}^{\mathrm{II}}) u_k^{\mathrm{II}}(\mathbf{x})\} \, \mathrm{d}\Gamma(\mathbf{x}), \tag{16}$$

with

$$\underline{C}_{ik}^{\mathrm{II}} = \begin{cases} \delta_{ik} & \mathbf{X} \in \Omega_{\mathrm{II}}, \\ \delta_{ik}/2, & \mathbf{X} \in \Gamma_{\mathrm{II}}, \\ 0, & \text{otherwise}. \end{cases} \tag{17}$$

All of the functions are defined for all $\mathbf{X}$ and are single-valued. Thus, we add (10) and (14), and (12) and (16) algebraically, and rearrange them in the following forms

$$\begin{aligned} &\underline{c}_{ij}^{\mathrm{I}}(\mathbf{X}) u_j^{\mathrm{I}}(\mathbf{X}) + \underline{c}_{ij}^{\mathrm{II}}(\mathbf{X}) u_j^{\mathrm{II}}(\mathbf{X}) \\ &\quad = \int_{\Gamma^{\mathrm{ex}}} \{u_{ij}^{*}(\mathbf{X}, \mathbf{x}) p_j(\mathbf{x}) - p_{ij}^{*}(\mathbf{X}, \mathbf{x}, \mathbf{n}) u_j(\mathbf{x})\} \, \mathrm{d}\Gamma(\mathbf{x}) \\ &\qquad + \int_{\Gamma^{c+a}} \{u_{ij}^{*}(\mathbf{X}, \mathbf{x})[p_j^{\mathrm{I}}(\mathbf{x}) + p_j^{\mathrm{II}}(\mathbf{x})] \\ &\qquad - [p_{ij}^{*}(\mathbf{X}, \mathbf{x}, \mathbf{n}^{\mathrm{I}}) u_j^{\mathrm{I}}(\mathbf{x}) + p_{ij}^{*}(\mathbf{X}, \mathbf{x}, \mathbf{n}^{\mathrm{II}}) u_j^{\mathrm{II}}(\mathbf{x})] \, \mathrm{d}\Gamma(\mathbf{x}), \end{aligned} \tag{18}$$

and

$$\begin{aligned} &\underline{C}_{ik}^{\mathrm{I}}(\mathbf{X})\sigma_{kj}^{\mathrm{I}}(\mathbf{X}) + \underline{C}_{ik}^{\mathrm{II}}(\mathbf{X})\sigma_{kj}^{\mathrm{II}}(\mathbf{X}) \\ &\quad = \int_{\Gamma^{\mathrm{ex}}} \{U_{ijk}^{*}(\mathbf{X}, \mathbf{x}) p_k(\mathbf{x}) - P_{ijk}^{*}(\mathbf{X}, \mathbf{x}, \mathbf{n}) u_k(\mathbf{x})\} \, \mathrm{d}\Gamma(\mathbf{x}) \\ &\qquad + \int_{\Gamma^{c+a}} \{U_{ijk}^{*}(\mathbf{X}, \mathbf{x})[p_k^{\mathrm{I}}(\mathbf{x}) + p_k^{\mathrm{II}}(\mathbf{x})] \\ &\qquad - [P_{ijk}^{*}(\mathbf{X}, \mathbf{x}, \mathbf{n}^{\mathrm{I}}) u_k^{\mathrm{I}}(\mathbf{x}) + P_{ijk}^{*}(\mathbf{X}, \mathbf{x}, \mathbf{n}^{\mathrm{II}}) u_k^{\mathrm{II}}(\mathbf{x})] \, \mathrm{d}\Gamma(\mathbf{x}), \end{aligned} \tag{19}$$

where the superscript ex denotes an external regular boundary, the superscript c denotes a crack boundary, and the superscript a denotes an artificial boundary generated by the cutting process. Moreover, the integrals over $\Gamma_{\mathrm{I}}^{\mathrm{ex}}$ and $\Gamma_{\mathrm{II}}^{\mathrm{ex}}$ have been put together with $\Gamma^{\mathrm{ex}} = \Gamma_{\mathrm{I}}^{\mathrm{ex}} + \Gamma_{\mathrm{II}}^{\mathrm{ex}}$; the superscripts I and II have been dropped since $\Gamma_{\mathrm{I}}^{\mathrm{ex}}$ and $\Gamma_{\mathrm{II}}^{\mathrm{ex}}$ do not overlap. Equilibrium of the whole structure indicates that the tractions on two coincident opposite artificial boundaries are equal in magnitude and opposite in direction; i.e.,

$$p_i^{\mathrm{I}}(\mathbf{x}) = -p_i^{\mathrm{II}}(\mathbf{x}), \quad \text{as } \mathbf{x} \in \Gamma^{a}. \tag{20}$$

Also, due to the requirement of continuity of the displacement components at the coincident points on the artificial boundaries, it holds that

$$u_i^{\mathrm{I}}(\mathbf{x}) = u_i^{\mathrm{II}}(\mathbf{x}), \quad \text{as } \mathbf{x} \in \Gamma^a. \tag{21}$$

Moreover, the integral kernels in (7) and (9) have the following properties

$$p_{ij}^*(\mathbf{X}, \mathbf{x}, -\mathbf{n}) = -p_{ij}^*(\mathbf{X}, \mathbf{x}, \mathbf{n}),$$

$$\text{i.e.,} \quad p_{ij}^*(\mathbf{X}, \mathbf{x}, \mathbf{n}^{\mathrm{I}}) = -p_{ij}^*(\mathbf{X}, \mathbf{x}, \mathbf{n}^{\mathrm{II}}), \quad \text{as } \mathbf{x} \in \Gamma^{c+a}, \tag{22}$$

$$P_{ijk}^*(\mathbf{X}, \mathbf{x}, -\mathbf{n}) = -P_{ijk}^*(\mathbf{X}, \mathbf{x}, \mathbf{n}),$$

$$\text{i.e.,} \quad P_{ijk}^*(\mathbf{X}, \mathbf{x}, \mathbf{n}^{\mathrm{I}}) = -P_{ijk}^*(\mathbf{X}, \mathbf{x}, \mathbf{n}^{\mathrm{II}}), \quad \text{as } \mathbf{x} \in \Gamma^{c+a}. \tag{23}$$

In deriving the above, the reversal of the outward normal $\mathbf{n}$ at the two coincident points on the crack and artificial boundaries has been applied

$$\mathbf{n}^{\mathrm{I}}(\mathbf{x}) = -\mathbf{n}^{\mathrm{II}}(\mathbf{x}) \quad \text{as } \mathbf{x} \in \Gamma^{c+a}. \tag{24}$$

Using (15), (17), and (20) through (23) to (18) and (19), we obtain

$$\begin{aligned} I_i(\mathbf{X}) \;=\; & \int_{\Gamma^{\mathrm{ex}}} \{u_{ij}^*(\mathbf{X}, \mathbf{x}) p_j(\mathbf{x}) - p_{ij}^*(\mathbf{X}, \mathbf{x}, \mathbf{n}) u_j(\mathbf{x})\} \, \mathrm{d}\Gamma(\mathbf{x}) \\ & + \int_{\Gamma^c} \{u_{ij}^*(\mathbf{X}, \mathbf{x})(p_j^+(\mathbf{x}) + p_j^-(\mathbf{x})) \\ & - p_{ij}^*(\mathbf{X}, \mathbf{x}, \mathbf{n}^+) u_j^+(\mathbf{x}) - u_j^-(\mathbf{x}))\} \, \mathrm{d}\Gamma(\mathbf{x}), \end{aligned} \tag{25}$$

with

$$I_i(\mathbf{x}) = \begin{cases} u_i(\mathbf{X}) & \mathbf{X} \in \Omega, \\ c_{ij}(\mathbf{X}) u_j(\mathbf{X}) & \mathbf{X} \in \Gamma_{\mathrm{ex}}, \\ c_{ij}^+(\mathbf{X}) u_j^+(\mathbf{X}) + c_{ij}^-(\mathbf{X}) u_j^-(\mathbf{X}) & \mathbf{X} \in \Gamma^c, \\ 0, & \text{otherwise} \end{cases} \tag{26}$$

and

$$\begin{aligned} J_{ij}(\mathbf{X}) \;=\; & \int_{\Gamma^{\mathrm{ex}}} \{U_{ijk}^*(\mathbf{X}, \mathbf{x}) p_k(\mathbf{x}) - P_{ijk}^*(\mathbf{X}, \mathbf{x}, \mathbf{n}) u_k(\mathbf{x})\} \, \mathrm{d}\Gamma(\mathbf{x}) \\ & + \int_{\Gamma^c} \{U_{ijk}^*(\mathbf{X}, \mathbf{x})(p_k^+(\mathbf{x}) + p_k^-(\mathbf{x})) \\ & - P_{ijk}^*(\mathbf{X}, \mathbf{x}, \mathbf{n}^+)(u_k^+(\mathbf{x}) - u_k^-(\mathbf{x}))\} \, \mathrm{d}\Gamma(\mathbf{x}), \end{aligned} \tag{27}$$

with

$$J_{ij}(\mathbf{X}) = \begin{cases} \sigma_{ij}(\mathbf{X}) & \mathbf{X} \in \Omega, \\ \sigma_{ij}(\mathbf{X})/2 & \mathbf{X} \in \Gamma_{\mathrm{ex}}, \\ (\sigma_{ij}^+(\mathbf{X}) + \sigma_{ij}^-(\mathbf{X}))/2 & \mathbf{X} \in \Gamma^c, \\ 0, & \text{otherwise}, \end{cases} \tag{28}$$

where the superscript $^+$ indicates one side of a crack, and the superscript $^-$ indicates the corresponding opposite side, instead of the superscripts I and II. The positive side of a crack may be chosen arbitrarily, for convenience. Equations (25) and (27) are so-called the *single-domain dual integral equations of a cracked structure*; in these equations the integrals are taken only along the regular external boundary and one side of a crack. The artificial boundaries that appeared due to the cutting process have been entirely eliminated from consideration. If a structure contains multiple cracks, the single-domain dual integral equations are given in the same forms as (25) and (27).

Equations (25) and (27) with a source point on the boundary, i.e., $\mathbf{X} \in \Gamma^{ex+c}$, are of the most importance, in the formulation of boundary integral equations for elastostatic problems. In formulating a general boundary integral method using (27), it is advantageous to use tractions instead of stresses since the number of unknowns can be reduced. If (27) are 'multiplied' on both sides by the outward normal at the boundary point $\mathbf{X}$ as usual the traction version of (27) with $\mathbf{X} \in \Gamma^{ex+c}$ can be obtained as

$$\begin{aligned} J_{ij}(\mathbf{X})n_j(\mathbf{X}) \;=\; & \int_{\Gamma^{ex}} \{U^*_{ijk}(\mathbf{X},\mathbf{x})\,p_k(\mathbf{x}) - P^*_{ijk}(\mathbf{X},\mathbf{x},\mathbf{n})u_k(\mathbf{x})\}n_j(\mathbf{X}) \\ & + \int_{\Gamma^c} \{U^*_{ijk}(\mathbf{X},\mathbf{x})(p^+_k(\mathbf{x}) + p^-_k(\mathbf{x})) \\ & - P^*_{ijk}(\mathbf{X},\mathbf{x},\mathbf{n}^+)(u^+_k(\mathbf{x}) - u^-_k(\mathbf{x}))\}n_j(\mathbf{X})\,\mathrm{d}\Gamma(\mathbf{x}). \end{aligned} \tag{29}$$

Note that, as $\mathbf{X} \in \Gamma^c$, $n_j(\mathbf{X})$ is taken to be the outward normal of the positive crack side, i.e., $n_j(\mathbf{X}) = n^+_j(\mathbf{X})$.

Note that on the crack surfaces, the tractions are self-equilibrating and hence

$$n^+_j(\mathbf{X})(\sigma^+_{ij}(\mathbf{X}) + \sigma^-_{ij}(\mathbf{X}))/2 = p^+_i(\mathbf{X}) \quad \text{and} \quad p^+_i(\mathbf{x}) + p^-_i(\mathbf{x}) = 0. \tag{30}$$

Equations (30) can be used to simplify (25), (27) and (29) when applying to cracks. In this case, traction and displacement jump on a crack may be regarded as independent variables in a numerical formulation, with the least unknowns.

3. Cohesive zone model for a crack in elastostatics

The dual-boundary integral equations in (25) and (29) are valid for the whole body. However, while the external boundary conditions are given explicitly, special attention must be paid to the crack boundaries as they evolve, particularly if the fracture process zone near the crack tip is to be modeled. In this section, we consider the application of the boundary element method to the two dimensional problem of a crack with a line fracture process zone. This model of the fracture process zone is motivated by the fact that in some materials such as concrete, brittle polymers, fiber-reinforced composites, tough ceramics and some alloys, the crack surfaces are usually not separated completely behind the (fictitious) crack tip. There exists a relatively long extension of the crack – variously called the wake zone, the bridging zone, or cohesive zone – where tractions can be transferred across the crack line. The mechanisms responsible for the development of this kind of a process zone can be bridging of long-chain molecules in polymers, bridging of fibers or whiskers in composites, interlocking of grain boundaries in alloys and ceramics, and so on. For these materials, the cohesive zone model of a crack

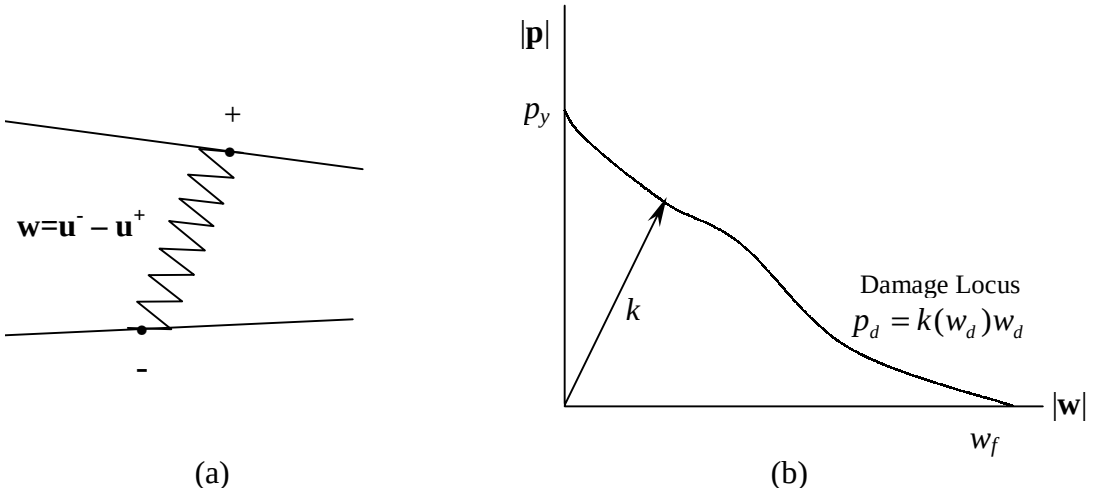

Figure 3. (a) Illustration of the two originally coincident points of a cohesive zone in the opening mode, connected by the line spring; (b) schematic diagram of the constitutive law of the line spring in terms of the traction and displacement jump. Note that instantaneous loading and unloading of the line spring is given by the slope k.

seems to be the appropriate model. The key assumption in this model is that material softening beyond the peak load is localized in a narrow layer behind a fictitious crack tip, whose volume is negligible and whose action is replaceable by cohesive forces. Typically, two types of constitutive laws are used in the literature for cohesive materials: one is characterized by a traction-displacement relationship, the other one by a material constitutive law defined in terms of stress and strain accompanied with a thickening law of the layer. In the latter, thickening of a cohesive layer is decoupled which may be worthy of studying separately in various materials considering rate-dependence and under dynamic loading. However, for quasistatic loading – the case considered predominantly in the literature – a law describing the traction-displacement relation is sufficient for modeling of the cohesive zone. We present below one such law for a cohesive crack represented by a line spring connecting two coincident crack points – this seems to be the most appropriate model for crazing-dominant brittle polymers and fiber-reinforced composites.

Consider a representation of the development of a crack shown in Figure 3(a). We suggest that two points, $\mathbf{x}^+$ and $\mathbf{x}^-$, originally coincident on opposite sides of a line, separate into two distinct points, connected by the cohesive zone material; continued straining increases the separation between these two points and eventually leads to cracking. The kinematics of this separation process are assumed to be described completely by the crack face separation, $\mathbf{w}$. Introducing the local normal and tangent directions at the cohesive zone tip, $\mathbf{w}$ can be resolved into the normal separation distance (or the cohesive zone opening displacement) component, $w_n = u_n^- - u_n^+$ and the tangential separation distance (or the sliding displacement) component $w_\tau = u_\tau^- - u_\tau^+$. In order to prevent the inter-penetration of the cohesive zone, $w_n \geqslant 0$; equality holds only in the case that there is contact between the top and bottom surfaces of the cohesive zone and in this case, we must also provide a description of the frictional resistance on the surface as well. We consider first the case of a locally opening mode crack with $w_n > 0$ and describe the force-separation law for the cohesive zone. The cohesive material may be modeled by a simple line spring that behaves according to the following

$$\mathbf{p} = k(w_d)\mathbf{w}, \tag{31}$$

or in component form

$$p_n = k(w_d)w_n, \qquad p_\tau = k(w_d)w_\tau, \tag{32}$$

where **p** is the traction vector with normal and tangential components, p_n and p_τ, respectively. w_d is the maximum separation distance between two originally coincident points on the crack over the entire loading history, and is used as a damage parameter. The stiffness of the cohesive zone material is denoted by $k(w_d)$ and is assumed to depend on the current state of damage. Note that $k(w_d)$ is a decreasing function of w_d, indicating the softening behavior of the material; this imposes an irreversibility of the damage process under unloading. Corresponding to each w_d, there exists a traction, p_d, and a damage locus derived from (31)

$$p_d = k(w_d)w_d. \tag{33}$$

The constitutive law described above is illustrated schematically in Figure 3(b). Note that the description of the cohesive zone material through the damage parameter and stiffness allows for irreversibility of damage. Upon unloading, the points on the cohesive zone unload linearly with a stiffness $k(w_d)$, whereas in most cohesive zone models, unloading occurs along the damage locus. Including the unloading effect has expanded the capability of the cohesive crack model in simulating realistic fracture behavior significantly. There are two critical states along the damage locus. The first one, at $w_d = 0$ and $p_d = p_y$, represents the maximum traction that can be sustained by the material before the cohesive zone begins to develop; beyond this critical level, separation processes begin and w_d increases. The point on the specimen that is at this state is usually called the fictitious crack tip or the cohesive zone tip. The second critical point on the damage locus occurs at $w_d = w_f$ and $p_d = 0$; this point represents the maximum displacement jump across the cohesive zone that can be sustained before cracking; beyond this level, the traction goes to zero and the two initially coincident points are now completely separated. The point on the specimen that is at this state is usually called the physical crack tip. Hence, (31) and (33) together, define the complete process of separation of a material point into a crack, as long as $w_n > 0$. A constitutive law in stress-strain for a cohesive material can be described in a similar manner (see Yang and Ravi-Chandar, 1996). The transition of that law to this law is apparent.

We now turn to the case when $w_n = 0$. Under arbitrary loading, contact of two crack surfaces could occur. In such cases, as shown in Figure 4a, we must provide an appropriate description for the development of friction along the cohesive zone, in addition to the line-spring model described above. We model the frictional interaction simply through a Coulomb type law. Thus, the tangential interaction of the crack surfaces in contact is given by

$$p_\tau = k(w_d)w_\tau - \mathrm{sgn}(w_\tau) f p_n, \tag{34}$$

where f is frictional coefficient. The equation for the determination of the normal component of the traction p_n is obtained by enforcing the contact condition $w_n = 0$. In (34), the first term represents the tangential traction contribution due to the line spring described above (nontrivially if it is not broken completely) and the second term represents the Coulomb friction component. In order to attain smooth transition of frictional force near $w_\tau = 0$, the frictional coefficient f may be assumed to be

$$f = \begin{cases} f_0 \dfrac{|w_\tau|}{w_{\tau d}}, & |w_\tau| \leqslant w_{\tau d}, \\ f_0, & \text{otherwise}. \end{cases} \tag{35}$$

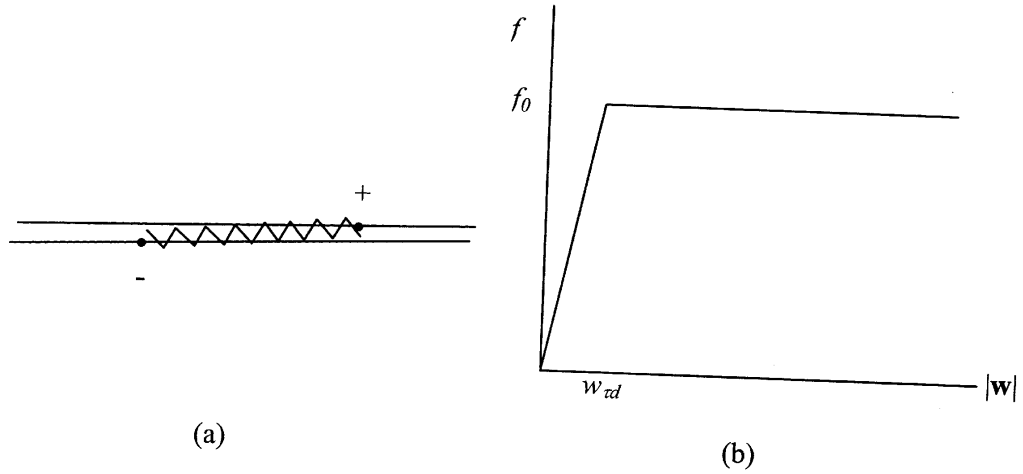

Figure 4. (a) Illustration of the two originally coincident points of a cohesive zone in the contact/sliding mode. The tangential interaction between the two points is modeled using Coulomb frictional force and the cohesive force if the cohesive line spring is not already broken; (b) sketch of the variation of the frictional coefficient of the contact surface.

where f_0 and $w_{\tau d}$ are both non-negative material constants. Function f is plotted in Figure 4(b). This completes the description of the cohesive zone material behavior.

There still remains the issue of deciding on the appropriate incorporation of this model into an elastostatic crack problem. One major question that arises is the following: *What is the criterion that can be used to grow the cohesive zone from a stress contentrator?* The incorporation of the cohesive zone model eliminates energy release criterion from consideration since the energy release rate will always be the same regardless of the direction of crack extension – it is simply the area under the damage locus, assuming a fully developed cohesive zone. The most plausible criteria, particularly for the line-spring nature of the cohesive zone mode, are stress based criteria such as the maximum principal stress criterion or the maximum tangential stress criterion at the fictitious crack tip. Assuming that one of these criteria would be appropriate, a second major question arises: *What should be the step size in extending the crack along this direction?* In finite element formulations, such as those of Xu and Needleman, (1994) and Ortiz (1996), cohesive zones are forced to develop along element boundaries and the extension is over the side of one entire element. The approach in these models is to make the element size so small that the overall crack growth behavior is captured adequately. In other words, the macroscopic crack path is suggested to be independent of the length scale of the discretization when the latter is sufficiently small compared to characteristic structural length scale. In the present work, we choose the maximum principal stress criterion for determining the crack increment. If the maximum principal stress at a fictitious crack tip reaches the critical value p_y, this tip is ready to run under further loading. The direction in which the tip advances is perpendicular to the direction of the maximum principal stress at that point, and the extension is such that the maximum principal stress at the new tip position is kept at the critical value p_y, during continued loading. However, note that, structural instability may occur while a crack is advancing; i.e., extension of a crack may enhance the stress state at a crack tip rather than release it. In this case, the crack may run fast and inertia effects may have to be included.

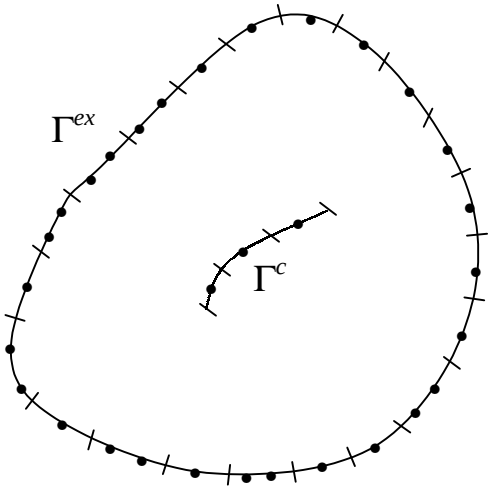

Figure 5. The discretization of the boundary into elements is shown in this figure. Each element contains one or more nodes distributed uniformly within the element. The nodes are internal to the element, indicating discontinuous elements.

4. Iterative boundary element method of successive over-relaxation

The behavior of the cohesive zone materials and the criterion for crack advance described in the last section require that an incremental loading procedure be used when solving boundary value problems. Moreover, an iteration process is indispensable in each loading step in general due to the fact that the constitutive law of the cohesive zone material, given in (31)–(35), involves irreversible damaging process, and is essentially history-dependent. Furthermore, the stiffness of the model line spring of the cohesive zone material $k(w_d)$, is in general a part of the solution, which may or may not be dependent on the current displacement discontinuity; in other words, there is no simple relationship between the traction and displacement discontinuity on a crack which may be used to achieve a linear system of equations to solve the problems numerically. Two strategies of iteration are possible in general: in the first, a linear system of equations of the discretized problem is formulated using the stiffness of the cohesive zone material obtained in the previous iteration step, and is solved by a typical solver either direct or iterative. The stiffness of the cohesive zone material is then modified based on this solution, and the process is repeated until the solution of the desired accuracy is achieved. In the second strategy, a nonlinear system of equations of the discretized problem is formulated using the stiffness of the cohesive zone material as unknowns, and is solved iteratively. By the first strategy, the iterative procedure is very clear and the convergence of the iteration process is expected. However, it is apparently time-consuming even with a very efficient solver of a linear system of equations; the linear system of equations is solved fully many times until a solution is achieved. On the other hand, the total time for a solution by the second strategy, if a good iterative procedure is found, would be in the same order as that for one step of the iteration by the first strategy (solving the linear system of equations once). In the present work, we adopt the second strategy and formulate an iterative method of successive over-relaxation for the present nonlinear problem of a cohesive crack. The solution procedure of this iterative method will be described below, following discretization of the boundaries and the boundary integral equations.

The boundaries of a cracked two-dimensional structure are approximated by straight elements, Γ_{el}s, of which each contains N_{el} nodes that are uniformly distributed in it, as shown in Figure 5. These nodes are numbered separately on the external boundary and on the crack locus. Assume that we have N^{ex} nodes on the external boundary and N^c nodes on the crack locus. A field quantity, $\mathbf{q}(\mathbf{x})$ can be approximated over an element Γ_{el} by interpolating the nodal values $\mathbf{q}^n$ in this element as

$$\mathbf{q}(\mathbf{x}) = \sum_{n=1}^{N_{\text{el}}} \phi^n(\mathbf{x})\mathbf{q}^n, \tag{36}$$

where the interpolation function, $\phi^n(\mathbf{x})$ satisfies the following conditions

$$\phi^n(\mathbf{x}^m) = \begin{cases} 1 & m = n, \\ 0 & m \neq n, \end{cases} \quad \text{and} \quad \sum_{n=1}^{N_{\text{el}}} \phi^n(\mathbf{x}) = \begin{cases} 1 & \mathbf{x} \in \Gamma_{\text{el}}, \\ 0 & \mathbf{x} \notin \Gamma_{\text{el}} \end{cases} \tag{37}$$

The interpolation functions may be constant, linear or quadratic, depending on the required accuracy of the representation. Substitute (36) into (25) and (29) with $\mathbf{X} \in \Gamma^{\text{ex}+c}$, the discretized forms of the dual boundary integral equations are obtained. Thus, one obtains

$$\sum_{n=1}^{N^{\text{ex}}} (g_{\alpha\beta}^{mn} p_\beta^n - h_{\alpha\beta}^{mn} u_\beta^n) + \sum_{n=N^{\text{ex}}+1}^{N^{\text{ex}}+N^c} h_{\alpha\beta}^{mn} w_\beta^n - I_\alpha(\mathbf{X}^m) = 0,$$
$$m = 1, 2, \ldots, N^{\text{ex}} + N^c \tag{38}$$

and

$$\sum_{n=1}^{N^{\text{ex}}} (G_{\alpha\beta}^{mn} p_\beta^n - H_{\alpha\beta}^{mn} u_\beta^n) + \sum_{n=N^{\text{ex}}+1}^{N^{\text{ex}}+N^c} H_{\alpha\beta}^{mn} w_\beta^n - J_{\alpha\beta}(\mathbf{X}^m) n_\beta(\mathbf{X}^m) = 0,$$
$$m = 1, 2, \ldots, N^{\text{ex}} + N^c. \tag{39}$$

Equations (38) and (39) each represent $2(N^{\text{ex}} + N^c)$ equations that are the discretized version of (25) and (29). In these equations, $g_{\alpha\beta}^{mn}$, $h_{\alpha\beta}^{mn}$, $G_{\alpha\beta}^{mn}$, and $H_{\alpha\beta}^{mn}$ are given explicitly by

$$g_{\alpha\beta}^{mn} = \int_{\Gamma^n} u_{\alpha\beta}^*(\mathbf{X}^m, \mathbf{x})\phi^n(\mathbf{x})\, \mathrm{d}\Gamma(\mathbf{x}), \tag{40}$$

$$h_{\alpha\beta}^{mn} = \int_{\Gamma^n} p_{\alpha\beta}^*(\mathbf{X}^m, \mathbf{x}, \mathbf{n})\phi^n(\mathbf{x})\, \mathrm{d}\Gamma(\mathbf{x}), \tag{41}$$

$$G_{\alpha\beta}^{mn} = \int_{\Gamma^n} U_{\alpha\delta\beta}^*(\mathbf{X}^m, \mathbf{x})\phi^n(\mathbf{x}) n_\delta(\mathbf{X}^m)\, \mathrm{d}\Gamma(\mathbf{x}), \tag{42}$$

$$H_{\alpha\beta}^{mn} = \int_{\Gamma^n} P_{\alpha\delta\beta}^*(\mathbf{X}^m, \mathbf{x}, \mathbf{n})\phi^n(\mathbf{x}) n_\delta(\mathbf{X}^m)\, \mathrm{d}\Gamma(\mathbf{x}), \tag{43}$$

where Γ^n is the element where the nth node is located. Equations (40) through (43) may be evaluated numerically if $\mathbf{X}^m \notin \Gamma^n$, and analytically if $\mathbf{X}^m \in \Gamma^n$. Note that the condition for a

self-equilibrating crack, Equation (30), has been used in the above equations. If **u** and **p**, are a trial set of displacements and tractions, Equations (38) and (39) would not be satisfied in general; instead, we obtain the following residuals

$$r_\alpha^m(\mathbf{u},\mathbf{p}) = \sum_{n=1}^{N^{\mathrm{ex}}}(g_{\alpha\beta}^{mn}\,p_\beta^n - h_{\alpha\beta}^{mn}\,u_\beta^n) + \sum_{n=N^{\mathrm{ex}}+1}^{N^{\mathrm{ex}}+N^c} h_{\alpha\beta}^{mn}\,w_\beta^n - I_\alpha(\mathbf{X}^m),$$

$$m = 1, 2, \ldots, N^{\mathrm{ex}} + N^c. \tag{44}$$

$$R_\alpha^m(\mathbf{u},\mathbf{p}) = \sum_{n=1}^{N^{\mathrm{ex}}}(G_{\alpha\beta}^{mn}\,p_\beta^n - H_{\alpha\beta}^{mn}\,u_\beta^n) + \sum_{n=N^{\mathrm{ex}}+1}^{N^{\mathrm{ex}}+N^c} H_{\alpha\beta}^{mn}\,w_\beta^n - J_{\alpha\beta}(\mathbf{X}^m)n_\beta(\mathbf{X}^m),$$

$$m = 1, 2, \ldots, N^{\mathrm{ex}} + N^c. \tag{45}$$

We call r_α^m the displacement residual and R_α^m the traction residual. If the residuals are close enough to zero, the trial set of **u** and **p** represents an approximate solution of the boundary value problem. At all regular boundary points, either the displacement or the traction vector components are prescribed; thus only one of (44) and (45) would be used in assembling the overall system of equations. For points that are in the cohesive zone, both the traction vector and the displacement discontinuity vector are unknown but related to each other through the constitutive description of the cohesive zone material provided in (31)–(35). From (45), for a point m that lies on the cohesive zone, the residual can be written as a relation between the displacement jump vector $\mathbf{w}(\mathbf{X}^m)$ and the traction vector $\mathbf{p}(\mathbf{X}^m)$. Note that points on the crack are simply special cases of the cohesive zone where the stiffness has decreased to zero and where $\mathbf{w}(\mathbf{X}^m)$ is unrestricted except that $w_n(\mathbf{X}^m) \geqslant 0$. Hence the complete set of all residuals at all nodal points can be calculated. Note that in order to incorporate the crack opening, crack sliding, and crack contact modes of deformation in a convenient way, field quantities in the discretized equations must be transformed into the local orthogonal coordinates in terms of the normal and tangential directions. We now turn to a description of an iterative solution scheme for solving (44) and (45) for **u** and **p**.

For a node m on the external boundary, either (44) or (45) could be used, depending on whether the imposed boundary condition at that point is a displacement or a traction condition. For the iterative solution scheme, in general, a field quantity $q_\alpha^{m,l+1}$ at the $(l+1)$th iteration is written in terms of its value at the lth iteration $q_\alpha^{m,l}$, and an increment that depends on the residuals as

$$q_\alpha^{m,l+1} = q_\alpha^{m,l} - \left.\frac{\overline{R}}{\partial\overline{R}/\partial q_\alpha^m}\right|^l, \tag{46}$$

where $\overline{R}$ is the appropriate residual for the field quantity q_α^m at the lth iteration. At the $(l+1)$th iteration step, the displacement component at this node $u_\alpha^{m,l+1}$, if not prescribed as a boundary condition, is calculated using the results at the lth iteration by

$$u_\alpha^{m,l+1} = u_\alpha^{m,l} + \omega r_\alpha^m(\mathbf{u},\mathbf{p})/(c_{\alpha\alpha}^m + h_{\alpha\alpha}^{mm}), \quad \text{(no sum on } \alpha), \tag{47}$$

where ω is an adjustable factor of relaxation. The displacement residual, $r_\alpha^m(\mathbf{u},\mathbf{p})$, is computed using the nodal values at the $(l+1)$th iteration step if available, or at the lth iteration

step. Similarly, a traction component $p_\alpha^{m,l+1}$, if not prescribed as a boundary condition, is calculated using the results at the lth iteration by

$$p_\alpha^{m,l+1} = p_\alpha^{m,l} + \omega R_\alpha^m(\mathbf{u}, \mathbf{p})/(0.5 - G_{\alpha\alpha}^{mm}), \quad \text{(no sum on } \alpha\text{)}, \tag{48}$$

where the traction residual R_α^m $(\mathbf{u}, \mathbf{p})$, is dealt with in the same way as r_α^m $(\mathbf{u}, \mathbf{p})$. For a node m which is on the cohesive zone, we calculate the displacement discontinuity $w_\alpha^{m,l+1}$, in opening mode by

$$w_\alpha^{m,l+1} = w_\alpha^{m,l} + \varpi\, R_\alpha^m(\mathbf{u}, \mathbf{p})/(k^{m,l} - H_{\alpha\alpha}^{mm}), \quad \text{(no sum on } \alpha\text{)}, \tag{49}$$

where ϖ is another adjustable factor of relaxation, and $k^{m,l}$ is calculated using (31) with $|\mathbf{w}^{m,l}|$. If the normal component of $\mathbf{w}$ at the $(l+1)$th iteration step $w_n^{m,l+1}$, is negative, it is set to be zero for no penetration of the crack surfaces. The tangential component of $\mathbf{w}$ at the $(l+1)$th iteration step $w_\tau^{m,l+1}$, is re-calculated by

$$w_\tau^{m,l+1} = w_\tau^{m,l} + \varpi\, R_\tau^m(\mathbf{u}, \mathbf{p})/(k^{m,l} - f_0 p_n^{m,l+1}/\bar{w}_{\tau d}| - H_{\tau\tau}^{mm}), \quad \text{(no sum on } \tau\text{)}, \tag{50}$$

where the frictional mode of the cohesive crack is activated; also $\bar{w}_{\tau d} = w_{\tau d}$ if $w_\tau^{m,l} \leqslant w_{\tau d}$; otherwise, $\bar{w}_{\tau d} = |w_\tau^{m,l}|$. Note that no special iterative process for mixed crack opening and contact is necessary.

We now describe the marching scheme used in the numerical solution; the solution procedure is implemented in three steps. Suppose that the solution at a previous loading step is already known. In order to solve the problem in the current loading step, first the cracked body is iterated to be in equilibrium with all the current cohesive nodes being held at the same displacement, using (47) and (48); in this step, the cohesive zone material law is not used. In the second step, the cohesive zone nodes are made free to displace according to the constitutive laws described above. The whole body is iterated again to be in equilibrium using (47) through (50). This holding and releasing process is found to produce quicker convergence for the iteration process than other schemes when a crack is advancing. The absolute difference of either displacement or traction at a boundary node between two next iteration steps is used to judge the convergence. The best relaxation factors of w and $\bar{w}$ can be obtained through some trial computations and these factors vary in general with the geometrical configuration of the body and loading conditions. Note that in the second step, the fictitious crack tip has not been allowed to move. After the equilibrium of the cracked body is obtained without crack advance, in the third step, stresses at a point of the fictitious crack tip are calculated using (27); note that a constant element is always used at the fictitious crack tip avoiding the difficulty of the integration due to the hypersingularity in the fundamental solution. If the maximum principal stress at this point is over the critical value, i.e. p_y, the fictitious crack tip is forced to advance a small increment in the direction perpendicular to the maximum principal stress. This is accomplished by increasing the length of the last cohesive tip element if it is smaller than a specific value and adding a new tip element otherwise. In this paper, we set the crack advance step to be equal to the cohesive zone tip element size; the ratio of the crack advance step to the crack element size could play a role in determining the local crack patterns in situations where the crack path is unstable, but this issue is not considered in this paper. Note that in general, a numerical stepwise scheme of crack advance may generate sharp corners between the approximating straight elements of a crack which may concentrate stresses; these stress concentrations are of a lower order than the crack tip concentration. Investigating the

role of these corners is of less interest than that of examining the crack tip; thus, in the present paper, we neglect the weaker corner singular point while dealing with a crack. Note also that at the current loading level, the above procedure of crack advance is repeated, and the iterative solution over whole body is obtained until the maximum principal stress is not above p_y at any point in the body. This procedure achieves the solution in the current loading step. The load is then incremented and the procedure repeated to march both the loading and the crack extension. In the following, we shall apply the method formulated above to some problems of a cohesive crack, and demonstrate the capacity of this method.

5. Applications

We turn to a demonstration of the capability of the boundary element strategy for handling of the cohesive cracks described above. In order to explore different aspects of the constitutive model for the cohesive zone that has been assumed in this paper, we consider three problems. The first problem concerns a single-edge-crack in a rectangular specimen under uniform far field tensile loading. For small initial crack lengths the crack extension in this configuration is unstable under displacement control; however, deep cracks exhibit stable crack growth. The results of this problem are discussed in Section 5.1. The second problem considered is that of an angled internal crack, under compressive loading; in this case, the cohesive zone develops contact and shear. The resulting path of the crack is the familiar wing crack pattern and is described in Section 5.2. The final problem considered is a demonstration of the capability of the formulation to handle mixed-mode crack growth and crack interaction; using the same loading as in the first problem, but with an offset double-edge crack configuration, the trajectories of the two edge cracks are tracked. The results, described in Section 5.3, show that the model duplicates the commonly observed behavior of two approaching cracks, and that the crack patterns exhibit a sort of bifurcation with the offset.

The following conditions describe the details of the simulation that are common to all three problems. The domain of interest is a rectangular two-dimensional region of length l and height h, taken equal to l in these simulations. In these simulations, all length quantities are normalized by l; while this is not a natural length scale for the fracture problem, it is convenient and easily interpreted. If it is desired, a scaling to an intrinsic length scale, such as the critical crack opening displacement for the cohesive zone w_f, may be effected easily. The deformation of the specimen is assumed to be in plane-strain. An initial process zone of length 0.02 is assumed to exist at the tip of all cracks in all simulations described in this paper; the damage parameter w_d is assumed to increase linearly from zero at the fictitious crack tip to w_f at the physical crack tip. Note that this initial damage zone can be prescribed arbitrarily and is in general unknown in the physical problem. The boundaries are discretized into discontinuous elements with a constant or quadratic interpolation over the element. Specifically, the straight-line segments on the external boundary are divided into 10 elements with quadratic interpolation; the length of each element is 0.1 and the nodal spacing is 0.0333. The initial crack (outside of the cohesive zone) is also divided into quadratic elements with a nodal spacing 0.01. The initial process zone is divided into equally-spaced elements of size 0.01 with quadratic interpolation, except for the element at the fictitious crack tip which is taken to be a constant element. When a fictitious crack tip advances, one new constant element of size 0.01 is added as the corresponding new fictitious crack tip element. The old fictitious crack tip element that is now an interior element within the cohesive zone is then redefined

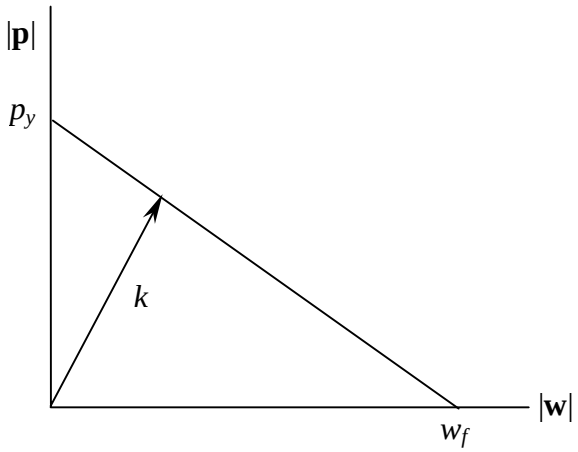

Figure 6. The two parameter constitutive law for the cohesive zone material used in the simulations.

as a quadratic element using three nodes inside it. The constitutive law of the cohesive crack is assumed to be represented by a straight line as shown in Figure 6, which is certainly the simplest one defined by the two parameters p_y and w_f; these parameters are taken to be $p_y = 0.01$ and $w_f = 0.001$. Note that all stress and traction quantities are normalized by μ. Poisson's ratio is taken to be 0.3. The unloaded specimen is initially in a stress free state. It is loaded incrementally in the direction perpendicular to the top and bottom boundaries under displacement control. The increment of the loading displacement is taken to be 1E-5 in tension and $-$1E-4 in compression. The relaxation factors were chosen initially by trial and error and were subsequently fixed at $\omega = 0.6$ and $\varpi = 1.4$.

In the following simulations, the boundary (including the cracks) is discretized into 150 to 350 nodes depending on the crack length resulting in a system of 300 to 700 equations (or degrees of freedom). In addition there are a few equations that provide the connection between tractions and crack opening displacements on the cohesive zone. If the stiffness of the cohesive zones is not modified by damage, for each loading step, fewer than 100 iteration steps are needed to achieve a solution to the system of equation, with an accuracy of 1E-8 in traction components and 1E-9 in displacement components. If the stiffness of the cohesive zones changes through damage, but still without propagation of the fictitious crack tips, slightly more than 100 iteration steps are required for each loading step. If a new cohesive element is added and accumulates damage, each loading step requires between 150 and 400 iteration steps. If the fictitious crack tip movement is sensitive to the load, quite a few new crack elements are added in one loading step; in this case, the required iteration steps may be as large as 1000, depending on the number of the new crack elements; fortunately, this does not happen often. We ran the code for the following problems on a Digital Alpha Workstation (200 4/100). Depending on the size of the discretized system, between 10 and 30 iteration steps can be performed in one second. Run times are as short as $\frac{1}{2}$ hours for small crack extensions; if long crack extensions are to be simulated the time required increases to the order of a few hours.

5.1. SINGLE EDGE CRACK UNDER TENSION

A number of simulations were performed with a single-edge-crack in the rectangular geometry shown in Figure 7. The crack was considered to be along the line of symmetry and its initial

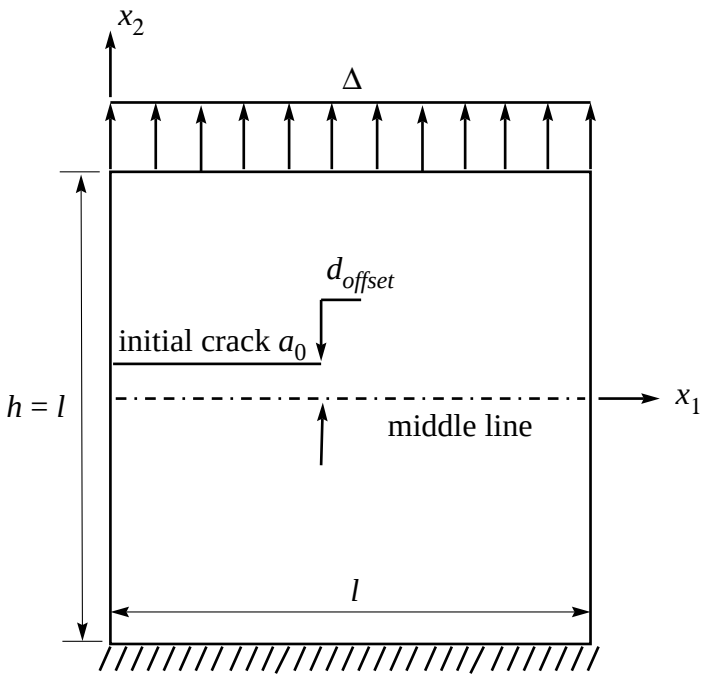

Figure 7. The configuration of a rectangular specimen with a single edge crack of initial length a_0, under displacement controlled elongation. This initial crack is parallel to the loading boundaries, and may be offset from the symmetry line in a distance.

length a_0, was varied from 0.03 to 0.78. The variation of the total load on the top boundary with the imposed elongation obtained from the simulations is shown in Figure 8. The main result, of course, is that in these simulations, simply by prescribing the applied loads and the cohesive law, initiation and growth of the crack appear naturally. These results are the mode-I analog of results that were obtained under mode III by Yang and Ravi-Chandar, (1998), using a finite difference scheme. A number of remarks regarding these simulations are listed below:

- During the loading process of a stable configuration, the fictitious crack tip starts to advance first. Note that the critical point of load at which the fictitious crack tip starts moving is of no significance since it is dependent on the initial state of the cohesive zone. With continued loading, the physical crack tip also starts to move. At this stage, the two crack tips advance at the same rate, keeping the size of the cohesive zone-defined as the distance between the fictitious and physical crack tips – a constant at about 0.1. This is considered to be the fully developed equilibrium cohesive zone size under this condition; of course, the size depends on the cohesive material model and the geometrical constraint imposed in the specimen.
- If the initial crack length a_0, is small, crack initiation is unstable even under displacement controlled loading. In the numerical procedure, this is manifested by the fact that the stress, calculated at a point ahead of the fictitious crack tip is larger than p_y even after the crack extension procedure has been applied over a length of many cohesive elements. This can also be inferred from the fact that the critical load for the onset of instability decreases with increasing initial crack length. Thus, crack extension and structural instability coincide in these cases. If the initial crack length is larger than about 0.48, crack extension is

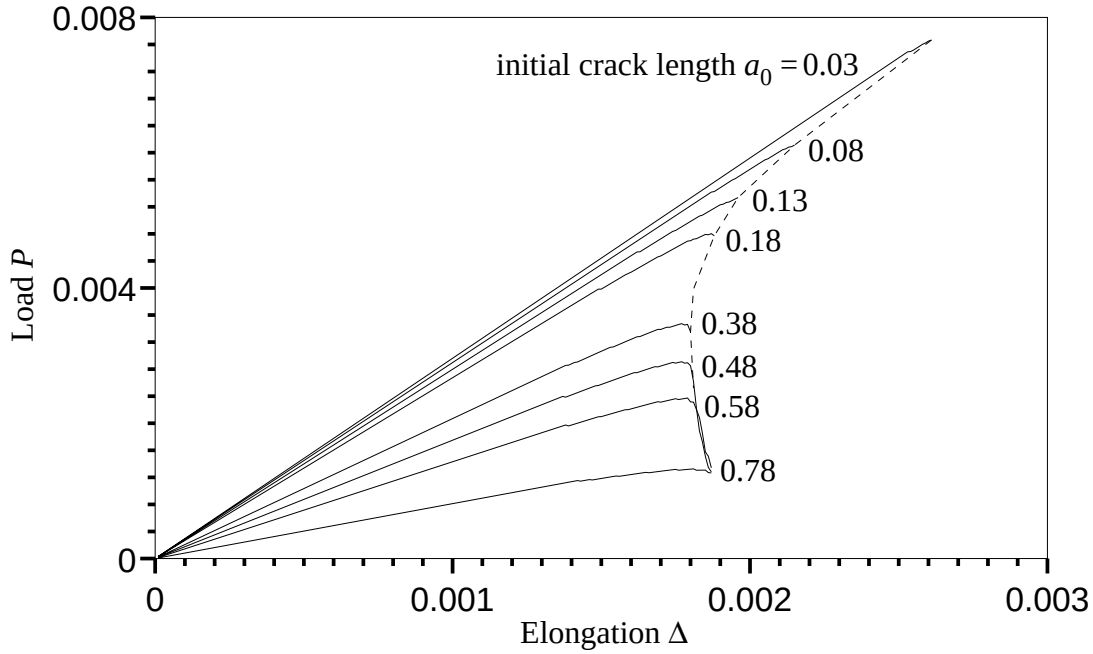

Figure 8. Load-elongation diagram of a set of simulations with a crack initially lying on $x_2 = 0$ and with a length a_0 from 0.03, to 0.78. An initial cohesive zone of size 0.02 is assumed in all the simulations. The crack growth is in the pure mode I. For $a_0 < 0.48$ approximately, crack extension is unstable under displacement control.

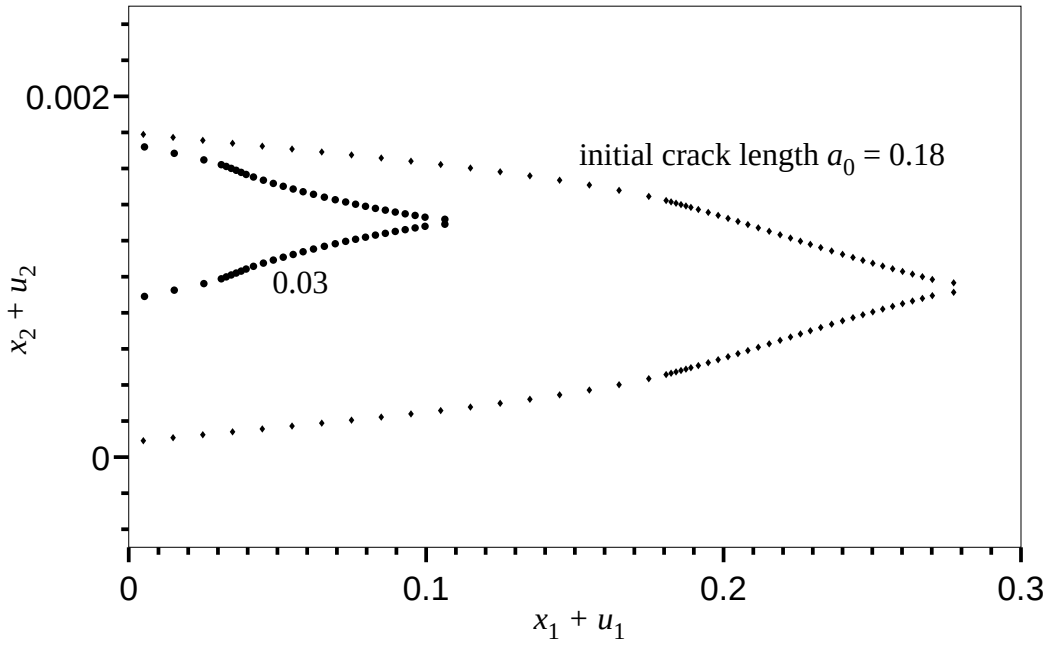

Figure 9. Crack opening profiles at the critical point of instability in two of the simulations for $a_0 = 0.03$ and 0.18.

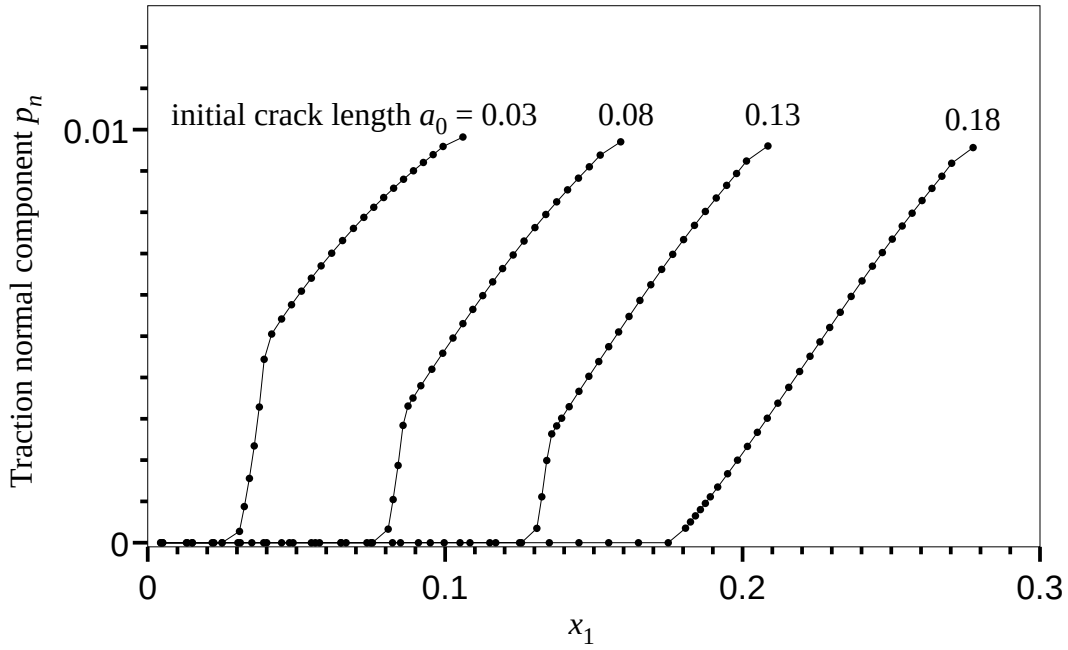

Figure 10. Traction normal component p_n along the cohesive zone at the critical point of instability in four of the simulations for $a_0 = 0.03$, 0.08, 0.13, and 0.18. The tangential component is zero indicating a pure opening mode for the cohesive zone. Note that, for very short initial crack lengths, the cohesive zones are not fully developed.

stable under displacement control. We examine later some issues related to crack paths in this range of stable crack growth. The behavior indicated by the sudden drop of load, for initial crack lengths less than 0.48 is usually referred to as a snap-back instability in structural mechanics. Note that the snap-back instability is also predicted by the stress intensity factor based linear elastic fracture mechanics and is simply a structural feature of this configuration; it is not influenced qualitatively by the fracture model.

- The evolution of the crack opening profiles and the cohesive tractions at the onset of unstable crack extension are shown in Figures 9 and 10 for a few initial crack lengths in the unstable region. Note that all these cracks had an initial cohesive zone of length 0.02 prior to load application. For long initial crack lengths, a steady-state cohesive zone of length 0.1 develops. However, for small initial crack lengths, at the onset of unstable crack extension, the cohesive zone is not completely developed. In other words, for short initial crack lengths, structural instability appears before development of a self-similar crack tip process zone. If the dissipation in the cohesive zone is computed, the result indicates that the dissipation is a function of crack length. Note that the data used for Figures 9 and 10 were obtained based on the numerical procedure of the loading displacement increment equal to 1E-5. A finer loading displacement increment may produce more developed cohesive zones representing their critical states instead of the ones plotted in Figures 9 and 10; however, this characteristic of incomplete development of the critical process zone at the onset of unstable crack initiation will not change. A similar behavior was identified in the mode III simulation by Yang and Ravi-Chandar (1998) and used to determine the range of applicability of a single parameter characterization of fracture.

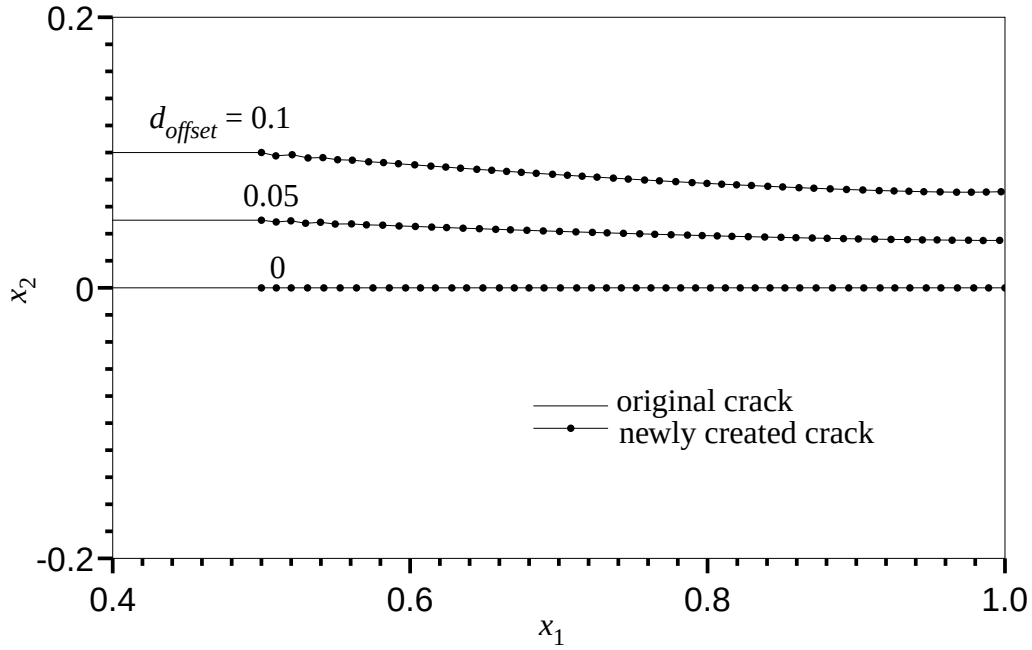

Figure 11. Crack trajectories in the simulations with different offsets of initial cracks. Nodes along the newly-created cracks are indicative of the new crack element ends.

In addition to the structural stability, the stability of the crack path is also of interest in crack problems. The single-edge-notched geometry used here is very stable to perturbations in the crack path. This is demonstrated by the results of the simulations shown in Figure 11. Here the crack paths obtained from three simulations are shown. The only difference between these simulations is that the edge crack is offset from the line of symmetry by d_{offset}. This offset, if nonzero, imposes a mixed-mode loading at the crack tip with the result that the crack path is no longer straight. The path stability of the crack is indicated by the fact that these cracks tend towards the line of symmetry. The main idea here is to demonstrate the capability of the present boundary element formulation to track arbitrary crack-path evolution. Further investigations into the influence of the loading on the crack-path stability are still under progress.

5.2. ANGLED CRACK UNDER COMPRESSION

The problem of cracks under compression has been of long-standing interest due to its importance in rocks and other brittle materials. Brace and Bombolakis (1963) made a crucial observation regarding the growth of angled cracks under compression: ‘crack growth occurred by the extension of the initial crack along a curving path which gradually became parallel with the direction of compression’. Moreover, the extension of the crack under compression was found to be stable even under prescribed loads. A number of other researchers have examined this problem since these early observations (see Nemat-Nasser and Horii, 1982, Steif, 1984, Horii and Nemat-Nasser, 1986). The overall objective in these studies has been to determine the stress intensity factors at the wing-crack tips so that a failure criterion based on a critical stress intensity factor criterion may be applied to determine the onset of crack extension. The analytical complications associated with such modeling forces one to assume a straight crack

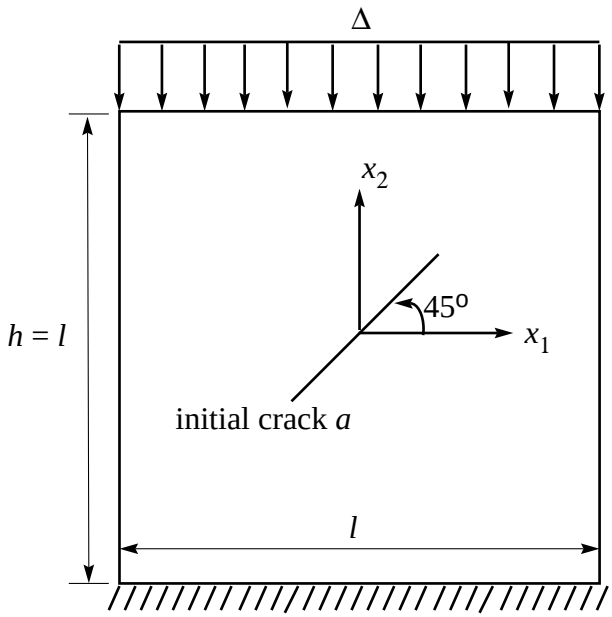

Figure 12. The loading configuration of a rectangular specimen with an internal crack inclined in an angle, subjected to displacement controlled compression.

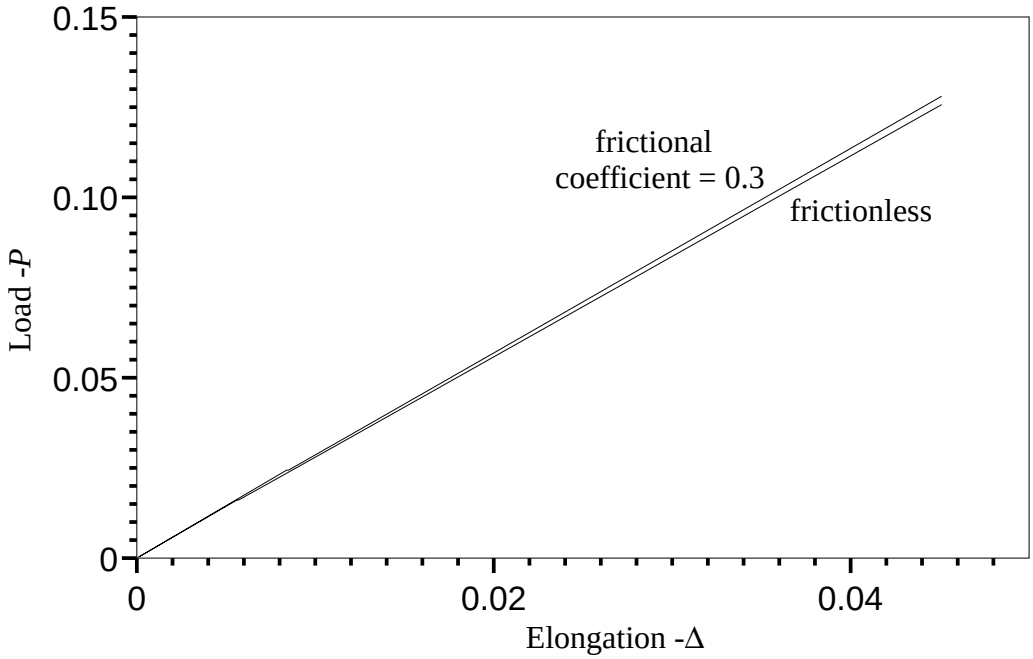

Figure 13. Comparison of the load-elongation curves with and without frictional force on the crack surfaces.

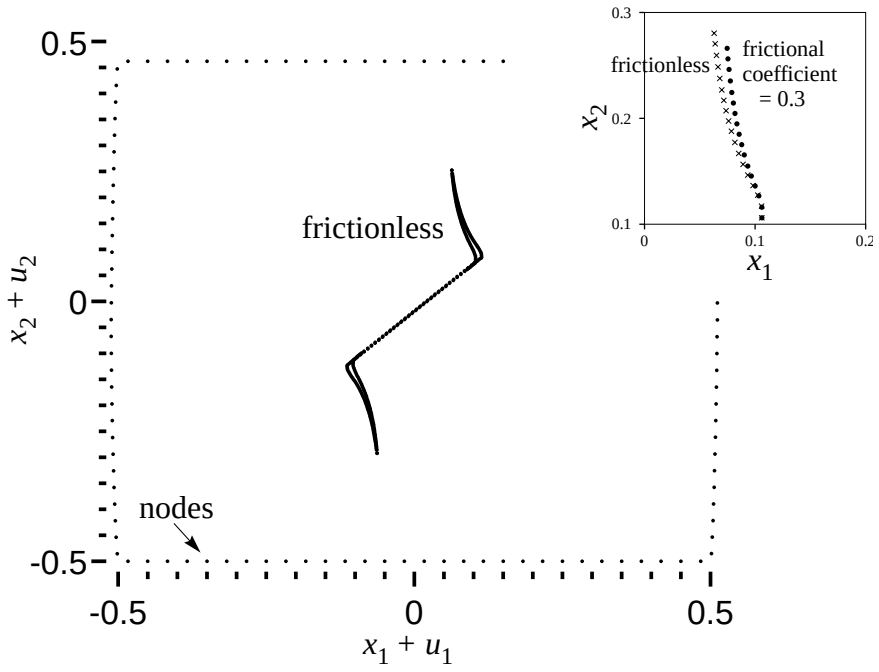

Figure 14. Deformed configuration of the specimen subjected to a compressive load of Δ equal to -0.04, without friction force on the crack surface. The wings are newly created cracks in opening mode. The final crack trajectories with and without frictional force on the crack surfaces are compared in the inset on the right and top corner, on the background of the original coordinates.

path, while experiments clearly indicate a curved path. We describe in this section, the result of a simulation using the cohesive zone formulation of the problem, where the evolution of the curved crack path is tracked completely, circumventing the calculation of local fracture parameters such as the stress intensity factor. Figure 12 shows the geometry of the angled crack problem in compression. The initial crack is taken to be 0.26 long and inclined at an angle 45°. As in the previous example, each physical crack tip is accompanied by an initial cohesive zone of size 0.02 along the direction of the initial crack, resulting in an overall crack length of 0.3. The cohesive zone model described in Section 3 is incorporated both with and without friction on the crack and cohesive surfaces. In the case with friction, the frictional coefficient f_0 is taken to be 0.3, and $w_{\tau d} = 1\text{E-}4$. The compressive loads are plotted against the imposed displacement in Figure 13. The deformed configuration at an applied displacement of -0.04 is shown in Figure 14 for the case without friction; also shown in the inset in this figure are the crack trajectories of the upper crack tips, comparing the differences introduced by including friction with a coefficient of 0.3. The main observations and results from the numerical simulations are summarized in the following list:

- Initiation of the fictitious crack tip occurs first; note that the advance of a fictitious crack tip is determined by the maximum principal stress criterion. After the cohesive zone is fully developed at a higher load, the physical crack tip starts to move, following the fictitious crack tip along the same path. In this early stages of the stable crack movement, the fully developed cohesive zone is of the size about 0.04.
- The load required for continued crack extension increases monotonically, with a very small change in the overall stiffness of the specimen. As can be seen from Figure 13, the

influence of friction on the global response is also small. Of course, the magnitude of the stiffness change is influenced by the dissipation assumed in the cohesive zone model for the crack. Note that the energy release rate for a stable crack in steady state – which is simply equal to $p_y w_f/2$ – was assumed to be 5E-6. At the imposed displacement of -0.04, the total dissipation due to the crack advance can be estimated to be three orders of magnitude smaller than the strain energy stored in this system. If the specimen is unloaded, only a very small loop of dissipation can be observed.

- Due to the continuous evolution of the stress field as the crack and cohesive zone extend, a curved path is followed. The influence of friction on the overall evolution of the crack path is also not very significant, as shown in Figure 14. The curved path bears a good resemblance to the path observed in experiments.
- After the crack path aligns itself parallel to the direction of compression, the crack does not extend further under increased global compression; the applied compression is transmitted through contact on the inclined initial cracks and the extended tips of the wing cracks appear not to be loaded any further. This can be understood simply by considering that the wing crack tips are parallel to the applied loading and hence do not generate a stress concentration at their tips. This observation is confirmed by the approximate solutions of Steif (1984) and Horii and Nemat-Nasser (1986b) which show the diminishing influence of the shearing of the original crack faces on the wing crack tip and the approach of the mode I stress intensity factor at the wing crack tip to zero as the wing crack length becomes long. For further failure of the block, other mechanisms, not included in this simulation, are responsible.
- After the cohesive zone is fully developed the cohesive zones at the tips of both cracks advance at the same rate. However, the size of the cohesive zone was found to decrease with continued loading; for instance, the cohesive zone size at the loading displacement of -0.04 is only about half of the full cohesive zone size 0.04 at the loading displacement of -0.015. This is explained by the effect of the component of the normal stress parallel to the crack (the T-stress). The large T-stress parallel to the growing wing crack suppresses the expansion of the cohesive zone.
- Note that in this problem, two crack and cohesive zone tips are involved, but the formulation of the boundary element method with a cohesive zone is able to track both tips without any additional complications in the numerical scheme.

5.3. Interaction of cracks in the double edge cracked specimen

The last problem we consider in this paper is a double-edge-crack loaded in tension allowing crack interaction. This problem also provides an opportunity to examine cracks that exhibit structural instability. The geometry of the specimen is shown in Figure 15. The initial lengths of the two edge-cracks, a_{1o} and a_{2o}, are both set equal to 0.28. Each crack tip is again provided with an initial cohesive zone of length 0.02. In order to examine the approach of the two cracks towards each other, an offset d_{offset} is provided between the two edge cracks. The load-elongation curves for two cases of d_{offset} equal to 0.1 and 0.2 respectively are shown in Figure 16. The deformed configurations showing the crack paths determined from the simulations are presented in Figure 17 and 18. The main observations and results are described as follows:

- Initiation of the fictitious and physical crack tips is very similar to the cases described in Section 5.1. Note that the full geometry of the specimen is modeled and the anti-symmetry

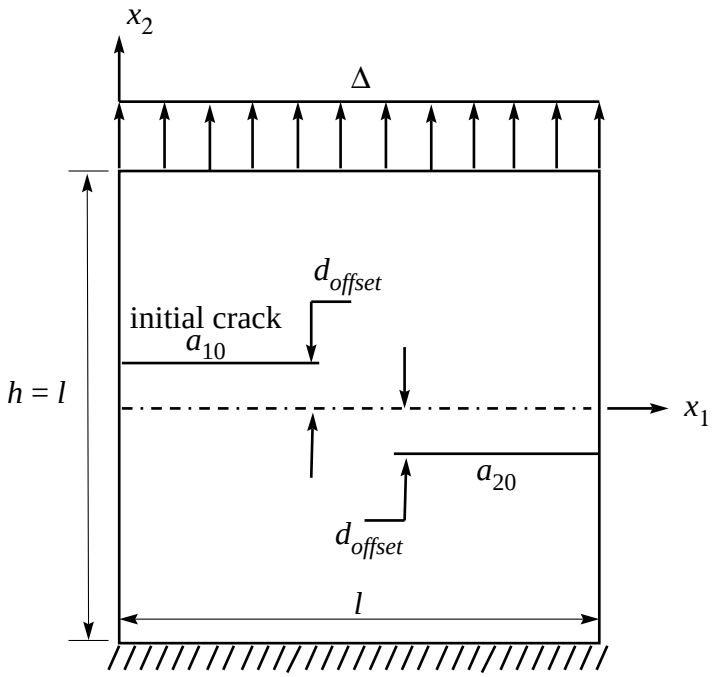

Figure 15. The loading configuration of a rectangular specimen with two edge cracks on the opposite sides, under displacement controlled elongation. The cracks are initially parallel to the loading boundaries, and may be offset from the symmetry line by an offset d_{offset}.

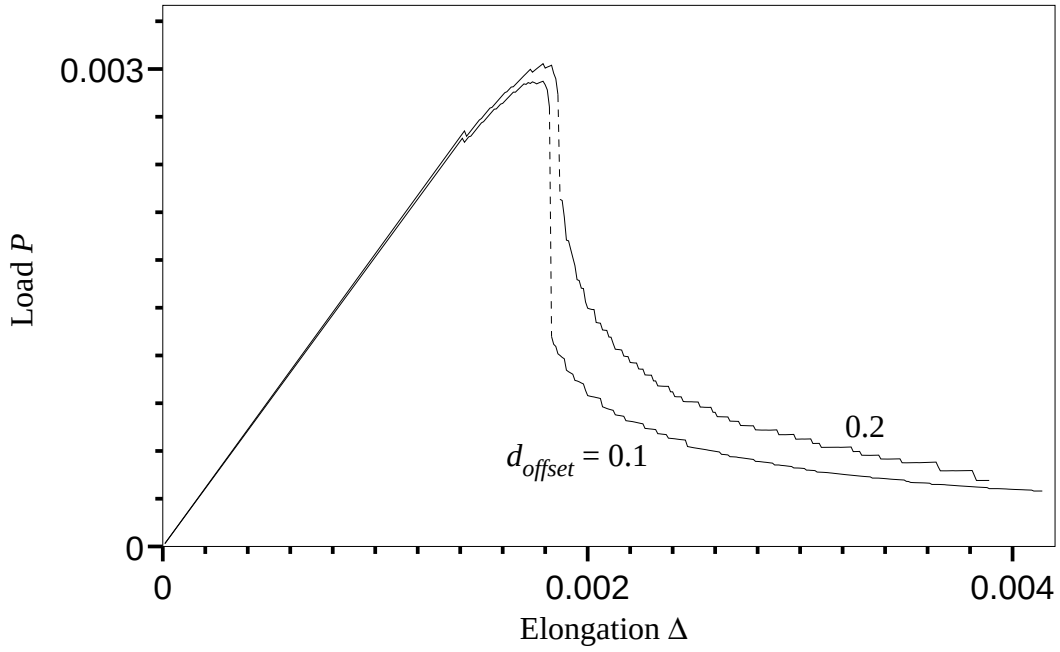

Figure 16. Load-elongation curves in the simulations of crack interaction with the offset d_{offset} as given above. Besides, the cracks $a_{10} = a_{20} = 0.28$ initially, and each crack tip was assumed to have an initial cohesive zone of size 0.02. The dashed lined indicate the loss of structural stability.

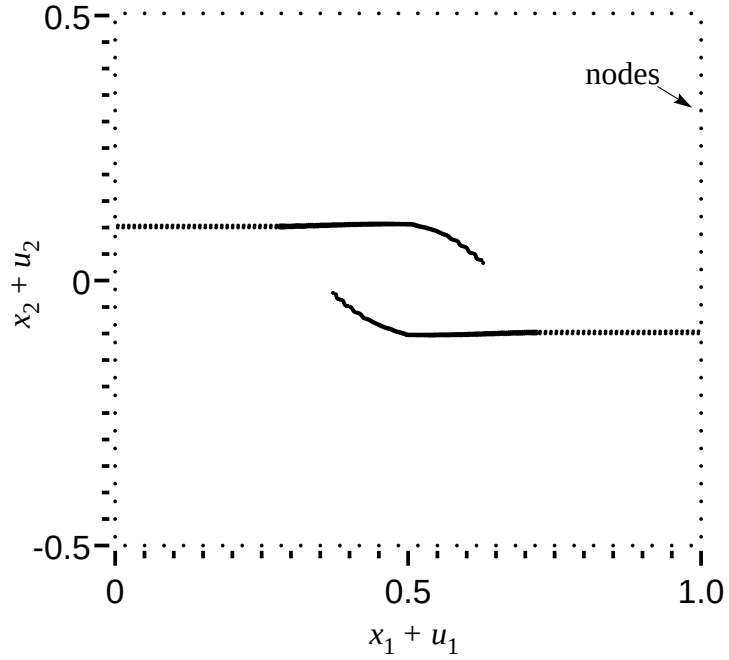

Figure 17. Deformed configuration of the specimen with two edge cracks with the offset $d_{\text{offset}} = 0.1$, corresponding to an extension $\Delta = 0.0038$.

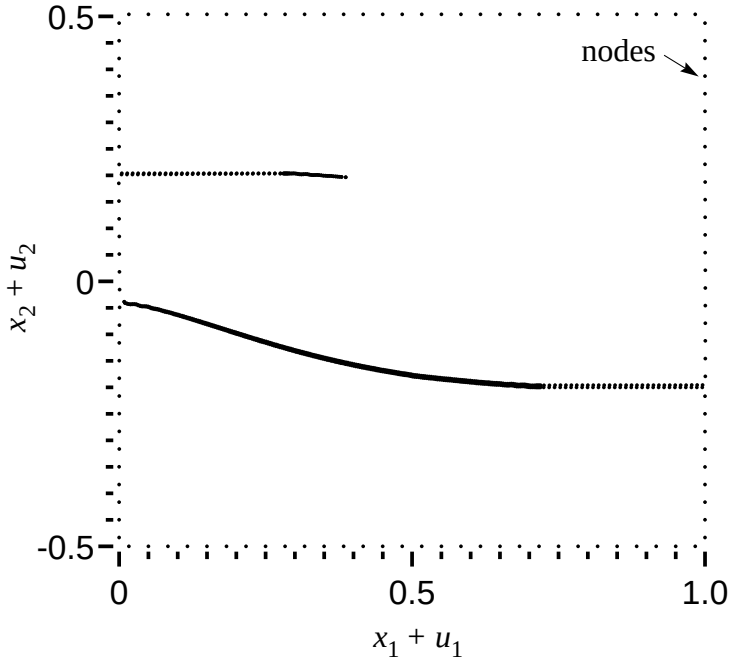

Figure 18. Deformed configuration of the specimen with two edge cracks with the offset $d_{\text{offset}} = 0.2$, corresponding to an extension $\Delta = 0.0038$.

of the offset cracks has not been imposed externally. For both cases, the cohesive ones at both crack tips are fully developed.

- For both simulations with $d_{\text{offset}} = 0.1$ and 0.2, after initial stable extension of both crack tips over a length of about 0.1, structural instability occurs and the equilibrium formulation of the problem may no longer be appropriate. At this point, the cohesive zone is fully developed. If we assume that the inertial effects are small in dictating the crack path, we may be able to determine the path evolution of these interacting cracks. We used the following strategy in our simulations to determine the crack extension behavior. At the onset of structural instability, the trajectory of the maximum principal stress from the crack tip is evaluated first; the cohesive zone – i.e., the fictitious and physical crack tips – is then extended along this predetermined path, at fixed global displacement, until the stress ahead of the fictitious crack tip falls to p_y so that stability is restored. After propagating the crack according to this strategy for a length of about 0.1, stability is restored. We note, however, that this scheme did not work very well when the offset was very small indicating that inertia effects may indeed be significant and should be taken into account.
- It is interesting to note that, in Figure 17 for $d_{\text{offset}} = 0.1$, the two cracks initially 'repel each other, pass over one another (overlap) and eventually approach each other along a curved path. This is very similar to the experimental observations of Melin (1983). On the other hand, in Figure 18 for $d_{\text{offset}} = 0.2$, the two crack tips 'attract' each other right from initiation. From a different point of view, the two crack tips approach the line of symmetry separately without much interaction in the early stages; we note that a single offset crack shows the tendency to approach the line of symmetry as demonstrated in Section 5.1. After initial extensions of the both cracks over a length of about 0.1 each, the left crack is completely shielded by the growth of the right-side crack and only one crack grows in this case. The change of crack patterns with d_{offset} is a bifurcation phenomenon of significant interest (see for example, Mulhaus et al., 1996). The bifurcation can be understood in the following terms: consider unequal extension of one of the crack tips due to perturbations. For cracks with small initial offset distances, perturbations in the development of either crack tip results in increased loading of the lagging crack tip while for large initial offset distances, these perturbations result in an increased loading at the leading crack tip.

6. Conclusions

A single-domain, dual-boundary integral formulation of elastostatic crack problems incorporating a cohesive zone model for the evolution of the fracture process is demonstrated in this paper. The cohesive zone is modeled as a damaging material with a prescribed behavior relating the applied force to the crack-opening displacement. The irreversible nature of the damage is introduced through the damage parameter w_d, the maximum displacement experienced by a point on the cohesive zone during its history. The introduction of the cohesive zone necessitates an iterative solution procedure to solve the equations resulting from the boundary integral formulation; the method of successive-over-relaxation is used in this study. In terms of numerical simulations, the approach described here presents significant advantages over grid-based finite element methods since the present formulation

(i) does not force development of the crack along element boundaries and thereby introduce mesh size and element geometry dependencies,
(ii) does not require fine nodal spacing except within the cohesive zone, and

(iii) does not require remeshing with crack extension.

Three example problems were considered to demonstrate the capability of this formulation to handle arbitrary in-plane crack problems, including mixed-mode problems, contact problems, and crack interaction problems.

Acknowledgments

The support of the Air Force Office of Scientific Research during the course of this work is gratefully acknowledged.

References

Aliabadi, M.H. (1997). Boundary element formulations in fracture mechanics. *Applied Mechanics Reviews* **50**, 83–96.

Ameen, Mohammed and Raghuprasad, B.K. (1994). A hybrid technique of modeling of cracks using displacement discontinuity and direct boundary element method. *International Journal of Fracture* **67**, 343–355.

Blandford, G.E., Ingraffea, A.R. and Liggett, J.A. (1981). Two-dimensional stress intensity factor computations using the boundary element method. *International Journal of Numerical Methods in Engineering* **17**, 387–404.

Brace, W.F. and Bonbolakis, E.G. (1963). A note on brittle crack growth in compression. *Journal of Geophysical Research* **68**, 3709–3713.

Brebbia, C.A., Telles, J.C.F. and Wrobel, L.C. (1984) *Boundary Element Techniques*: *Theory and Applications in Engineering*, Springer-Verlag.

Chen, W.H. and Chen, T.C. (1995). An efficient dual boundary element technique for a two-dimensional fracture problem with multiple cracks. *International Journal of Numerical Methods in Engineering* **38**, 1739–1756.

Crouch, S.L. (1976). Solution of plane elasticity problems by the displacement discontinuity method. *International Journal of Numerical Methods in Engineering* **10**, 301–342.

Cruse, T.A. (1996). BIE fracture mechanics analysis: 25 years of developments. *Computational Mechanics* **18**, 1–11.

Hartmann, F. (1980). Computing the C-matrix in non-smooth boundary points. In: *New Developments in Boundary Element Methods*. (Edited by Brebbia, C.A.), Butterworths, London, 367–379.

Hong, H. and Chen, J. (1988). Derivations of integral equations of elasticity. *Journal of Engineering Mechanics* ASCE, **114**, 1028–1044.

Horii, H. and Nemat-Nasser, S. (1986). Brittle failure in compression: Splitting, faulting and brittle-ductile transitions. *Philosophical Transactions of the Royal Society of London* **A319**, 337–374.

Love, A.E.H. (1944). *A Treatise on the Mathematical Theory of Elasticity*, Dover, New York.

Melin, S. (1983). Why do cracks avoid each other? *International Journal of Fracture* **23**, 37–45.

Mulhaus, H.-B., Chau, K.T. and Ord, A. (1996). Bifurcation of crack pattern in arrays of two-dimensional cracks. *International Journal of Fracture* **77**, 1–14.

Nemat-Nasser, S.N. and Horii, H. (1982). Compression-induced nonplanar crack extensionwith application to splitting, exfoliation and rockburst. *Journal of Geophysical Research* **87**, 6805–6821.

Ortiz, M. (1996). Computational micromechanics. *Computational Mechanics* **18**, 321–338.

Portela, A., Aliabadi, M.H. and Rooke, D.P. (1991). The dual boundary element method: effective implementation for crack problems. *International Journal of Numerical Methods in Engineering* **33**, 1269–1287.

Snyder, M.D. and Cruse, T.A. (1975). Boundary integral equation analysis of cracked anisotropic plates. *International Journal of Fracture* **11**, 315–342.

Steif, P.S. (1984). Crack extension under compressive loading. *Engineering Fracture Mechanics* **20**, 463–473.

Wen, P.H. (1996). Dynamic fracture mechanics: Displacement discontinuity method, Computational Mechanics Publications.

Xu, X.-P. and Needleman, A. (1994). Numerical simulations of fast crack growth in brittle solids. *Journal of Mechanics and Physics of Solids* **42**, 1397–1434.

Yang, B. and Ravi-Chandar, K. (1996). On the role of the process zone in dynamic fracture. *Journal of the Mechanics and Physics of Solids* **44**, 1955–1976.

Yang, B. and Ravi-Chandar, K. (1998). Anti-plane shear crack growth under quasistatic loading in a damaging materials. *International Journal of Solids and Structures* **35**, 3695–3715.
Young, A. (1996). A single-domain boundary element method for 3-d elastostatic crack analysis using continuous elements. *International Journal of Numerical Methods in Engineering* **39**, 1265–1293.